ChemPubSoc Europe

DOI: 10.1002/chem.201402391

CHEMISTRY
A European Journal
Full Paper

Nickel Complexes

Nickel(II) Complexes of Pentadentate N5 Ligands as Catalysts for Alkane Hydroxylation by Using *m*-CPBA as Oxidant: A Combined Experimental and Computational Study**

Muniyandi Sankaralingam,[a] Mani Balamurugan,[a] Mallayan Palaniandavar,*[a, c] Prabha Vadivelu,*[b] and Cherumuttathu H. Suresh[b]

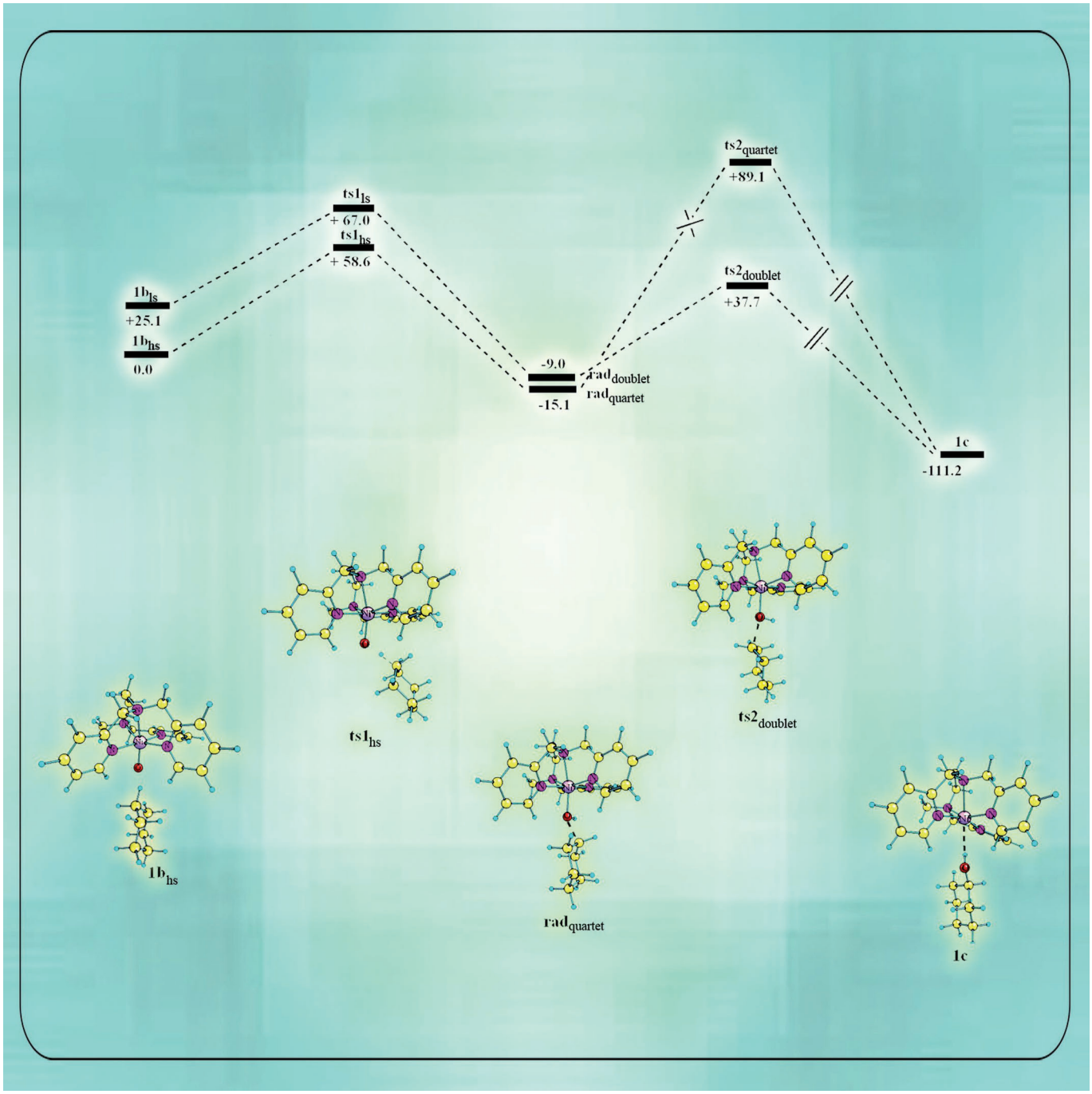

© 2014 Wiley-VCH Verlag GmbH & Co. KGaA, Weinheim

Abstract: A new family of nickel(II) complexes of the type $[Ni(L)(CH_3CN)](BPh_4)_2$, where L = *N*-methyl-*N*,*N*′,*N*′-tris(pyrid-2-ylmethyl)-ethylenediamine (L1, **1**), *N*-benzyl-*N*,*N*′,*N*′-tris(pyrid-2-yl-methyl)-ethylenediamine (L2, **2**), *N*-methyl-*N*,*N*′-bis(pyrid-2-ylmethyl)-*N*′-(6-methyl-pyrid-2-yl-methyl)-ethylenediamine (L3, **3**), *N*-methyl-*N*,*N*′-bis(pyrid-2-ylmethyl)-*N*′-(quinolin-2-yl-methyl)-ethylenediamine (L4, **4**), and *N*-methyl-*N*,*N*′-bis(pyrid-2-ylmethyl)-*N*′-imidazole-2-ylmethyl)-ethylenediamine (L5, **5**), has been isolated and characterized by means of elemental analysis, mass spectrometry, UV/Vis spectroscopy, and electrochemistry. The single-crystal X-ray structure of $[Ni(L3)(CH_3CN)](BPh_4)_2$ reveals that the nickel(II) center is located in a distorted octahedral coordination geometry constituted by all the five nitrogen atoms of the pentadentate ligand and an acetonitrile molecule. In a dichloromethane/acetonitrile solvent mixture, all the complexes show ligand field bands in the visible region characteristic of an octahedral coordination geometry. They exhibit a one-electron oxidation corresponding to the Ni^{II}/Ni^{III} redox couple the potential of which depends upon the ligand donor functionalities. The new complexes catalyze the oxidation of cyclohexane in the presence of *m*-CPBA as oxidant up to a turnover number of 530 with good alcohol selectivity (A/K, 7.1–10.6, A = alcohol, K = ketone). Upon replacing the pyridylmethyl arm in $[Ni(L1)(CH_3CN)](BPh_4)_2$ by the strongly σ-bonding but weakly π-bonding imidazolylmethyl arm as in $[Ni(L5)(CH_3CN)](BPh_4)_2$ or the sterically demanding 6-methylpyridylmethyl ($[Ni(L3)(CH_3CN)](BPh_4)_2$ and the quinolylmethyl arms ($[Ni(L4)(CH_3CN)](BPh_4)_2$, both the catalytic activity and the selectivity decrease. DFT studies performed on cyclohexane oxidation by complexes **1** and **5** demonstrate the two spin-state reactivity for the high-spin $[(N5)Ni^{II}–O^{\bullet}]$ intermediate ($ts1_{hs}$, $ts2_{doublet}$), which has a low-spin state located closely in energy to the high-spin state. The lower catalytic activity of complex **5** is mainly due to the formation of thermodynamically less accessible *m*-CPBA-coordinated precursor of $[Ni^{II}(L5)(OOCOC_6H_4Cl)]^+$ (**5a**). Adamantane is oxidized to 1-adamantanol, 2-adamantanol, and 2-adamantanone (3°/2°, 10.6–11.5), and cumene is selectively oxidized to 2-phenyl-2-propanol. The incorporation of sterically hindering pyridylmethyl and quinolylmethyl donor ligands around the Ni^{II} leads to a high 3°/2° bond selectivity for adamantane oxidation, which is in contrast to the lower cyclohexane oxidation activities of the complexes.

Introduction

The selective oxidation of saturated hydrocarbons under mild conditions is an exciting and challenging scientific goal and has received great attention in recent years. The conventional hydroxylation processes usually require high temperatures and high pressures and will give only a mixture of alcohol and aldehyde/ketone as the over-oxidized product. On the other hand, oxo-iron units in many mono- and dioxygenase enzymes catalyze these reactions very efficiently with high selectivity under mild reaction conditions; hence the enzymatic reactions follow methodologies different from those of conventional processes. The mostly used considerable metal-based oxidants are transition-metal oxo species, which are often suggested as reactive intermediates in various oxidation reactions ranging from industrial processes to biological systems.[1–6] Though iron complexes are considered to be one of the most promising catalysts, a variety of compounds of transition metals like Mn, Co, Cu, Ru, and Os is being investigated as catalysts for the alkane oxidation.[7–18] The very recently developed nickel dioxygen complexes, such as $[Ni^{III}_2(\mu\text{-}O)_2]$, which exhibit hydrogen abstraction from aliphatic carbon atoms in a manner similar to the high-valent $[Fe^{IV}_2(\mu\text{-}O)_2]$ and $[Cu^{III}_2(\mu\text{-}O)_2]$ species, have thrown light on the applicability of nickel complexes as oxidizing agents.[19–23] Also, several oxo-bridged dinuclear Ni^{II} complexes have been reported to be involved in dioxygen activation chemistry.[24–34]

In addition, theoretical investigations on alkane hydroxylation catalyzed by the first-row transition-metal oxide ions have revealed the alkane hydroxylation potential of metal–oxygen species.[35] Itoh et al. have shown[36] that the Ni^{II} complex $[Ni(TPA)(OAc)(H_2O)](BPh_4)$, where TPA is tris(pyrid-2ylmethyl)amine and OAc is acetate, is a very efficient, alcohol-selective, and robust turnover catalyst for alkane hydroxylation with *m*-chloroperbenzoic acid (*m*-CPBA) as oxidant. They have isolated a series of Ni^{II} complexes of linear N3 and tripodal N4 and tripodal monophenolate (N3O) ligands and studied the effect of the ligand and the counter anion on the catalytic oxidation of cyclohexane by using *m*-CPBA. They have suggested that the highly reactive nickel-oxo ($Ni{=}O^+$) intermediate rather than an auto-oxidation-type free radical species is involved in the catalytic cycle.[37] Also, they have reported Ni^{II} complexes of tripodal bis- and tris(phenolate) ligands, which are capable of catalyzing the oxidation of cyclohexane to cyclohexanol by using *m*-CPBA with up to 100% conversion based on the oxidant under solvent-free conditions.[38] Hikichi et al. have crystal-

[a] *Dr. M. Sankaralingam, Dr. M. Balamurugan, Prof. Dr. M. Palaniandavar*
School of Chemistry, Bharathidasan University
Tiruchirappalli—620024, Tamil Nadu (India)
E-mail: palanim51@yahoo.com, palaniandavarm@gmail.com

[b] *Dr. P. Vadivelu, Dr. C. H. Suresh*
Chemical Sciences and Technology Division
CSIR-National Institute for Interdisciplinary Science and Technology
Trivandrum—695019. (India)
E-mail: prabha135@gmail.com

[c] *Prof. Dr. M. Palaniandavar*
Department of Chemistry
Central University of Tamil Nadu
Thiruvarur—610001, Tamil Nadu, (India)

[**] m-*CPBA* = m-*chloroperbenzoic acid.*

Supporting information for this article is available on the WWW under http://dx.doi.org/10.1002/chem.201402391.

© 2014 Wiley-VCH Verlag GmbH & Co. KGaA, Weinheim

lized the nickel(II) alkylperoxo complex [$Ni^{II}(Tp^{ipr})(OOtBu)$], where Tp^{ipr} is hydrotris(3,5-di-2-propylpyrazolyl)borate and *t*Bu is *tert*-butyl, and studied its catalytic oxidation activity towards alkanes.[39a] The same group has found[39b,c] that nickel(II) acylperoxo species are relevant to the catalytic alkane hydroxylation with *m*-CPBA. Very recently, we have isolated[40a] a few nickel(II) complexes of tripodal N4 ligands and also a few mixed ligand Ni^{II} complexes[40b] as catalysts for alkane hydroxylation reaction by using *m*-CPBA as the oxidant and studied the effect of stereoelectronic factors of the ligand of the catalysts upon the catalytic efficiency as well as the alcohol product selectivity. Interestingly, we obtained a linear correlation between the metal–ligand covalency parameter (β) and the total turnover number (TON). K. Ray et al.[41] trapped Ni^{III}=O/Ni^{III}–OH intermediate species in the reaction of a nickel(II) salt with *m*-CPBA and characterized them by using EPR and UV/Vis spectral techniques. However, the factors determining the formation and stabilization of the reactive intermediate species remain still unclear.

All the above-described observations reveal that nickel-oxo species are potential transition-metal catalysts for an efficient alkane hydroxylation reaction. So, we are prompted to continue to isolate nickel(II) complexes of N5 ligands (Scheme 1), probe the effect of stereoelectronic factors of the ligand on the formation and stability of the oxo-nickel species, and study their catalytic efficiency and alcohol selectivity in alkane hydroxylation. Here we report a few nickel(II) complexes of systematically varied pentadentate N5 ligands the pyridyl (py), the imidazolyl (im), and the sterically hindering 6-methylpyridyl/quinolyl moieties of which are expected to influence the electronic properties and the catalytic activities of the Ni^{II} complexes towards alkane hydroxylation. We intend to examine the effect of increasing the denticity from four as in the above-mentioned Ni^{II} complexes of N4 ligands[40a] to five as in the present complexes on the catalytic activity towards alkane hydroxylation. It is expected[37,40b] that an increase in denticity from four to five and the consequent increase in the ligand field strength would enhance the catalytic efficiency and selectivity. Also, we wish to collect evidences for the involvement of reactive intermediates in alkane hydroxylation reaction. We have found that all the complexes catalyze the hydroxylation of alkanes like cyclohexane and adamantane efficiently with good alcohol/ketone selectivity, in the presence of *m*-CPBA as oxidant within two hours. Also, all the complexes catalyze the selective oxidation of cumene to 2-phenyl-2-propanol. To illustrate the mechanism of the hydroxylation reactions and to throw light on the reactive nickel-oxo intermediates a DFT study has been undertaken for the first time, as the present octahedral complexes with N5 ligand are convenient for studying intermediate Ni-oxo species.

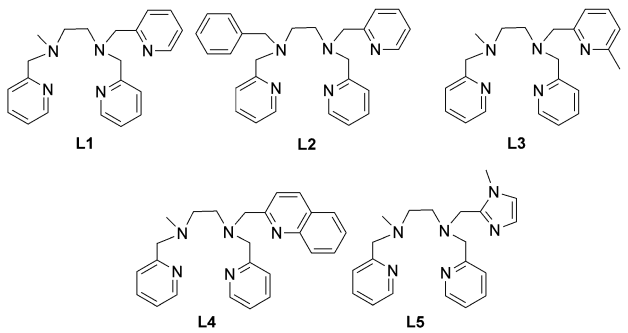

Scheme 1. Structures of the pentadentate N5 ligands employed in the study.

Results and Discussion

Synthesis and characterization of ligands and their nickel(II) complexes

The new pentadentate N5 ligands were synthesized according to known procedures involving Schiff base condensation and reductive amination with suitable modifications.[42,43] The ligands L1 and L2 were synthesized by reductive amination of *N*-methylethylenediamine (L1)/*N*-benzylethylenediamine (L2) with three equivalents of pyridine-2-carboxaldehyde by using sodium triacetoxyborohydride. The ligands L3–L5 were synthesized by Schiff base condensation of *N*-methylethylenediamine with 6-methylpyridine-2-carboxaldehyde (L3)/quinoline-2-carboxaldehyde (L4)/1-methylimidazole-2-carboxaldehyde (L5) followed by reduction with $NaBH_4$ and then reductive amination of two equivalents of pyridine-2-carboxaldehyde by using sodium triacetoxyborohydride. All the ligands were characterized by ^{1}H NMR spectroscopy and mass spectrometry. The nickel(II) complexes **1**–**5** were prepared by adding one equivalent of ligand to a solution of $[Ni(ClO_4)_2]\cdot 6H_2O$ in methanol, followed by the addition of sodium tetraphenylborate. They are formulated as $[Ni(L)(CH_3CN)](BPh_4)_2$ on the basis of elemental analysis, UV/Vis spectroscopy, ESI-MS and X-ray crystal structure analysis of complex **3**.

Description of the structure of $[Ni(L3)(CH_3CN)](BPh_4)_2$ (3)

The molecular structure of $[Ni(L3)(CH_3CN)](BPh_4)_2$ (**3**) is shown in Figure 1 together with the atom numbering scheme and the selected bond lengths and bond angles are collected in Table 1. The complex molecule contains a NiN_6 coordination sphere with a distorted octahedral coordination geometry constituted by three pyridine and two tertiary amine nitrogen atoms of the linear pentadentate ligand and an acetonitrile molecule. The Ni–N_{py} (2.0451–2.1692 Å) and Ni–N_{amine} (1.926-2.196 Å) bond lengths are in the ranges observed for previously reported nickel(II) complexes (Ni–N_{py}, 2.098–2.143, Ni–N_{amine}, 2.099–2.138 Å).[36–38,40] The Ni–$N4_{py}$ bond (2.098(2) Å) is shorter than the Ni–N_{amine} bonds (2.099(2), 2.138(2) Å) due to sp^2 and sp^3 hybridizations of the pyridyl and amine nitrogen donor atoms respectively. However, the Ni–$N1_{py}$ bond (2.141(2) Å) is longer than the Ni–N_{amine} bond due to the *trans* effect exerted by the pyridyl N1 nitrogen atom. The Ni–$N5_{py}$ bond is longer than the Ni–$N4_{py}$ and Ni–$N1_{py}$ bonds (2.098(2), 2.141(2) Å) due to the sterically hindering methyl substituent adjacent to the pyridine nitrogen atom. The Ni–$N6_{ACN}$ bond is shorter than all

© 2014 Wiley-VCH Verlag GmbH & Co. KGaA, Weinheim

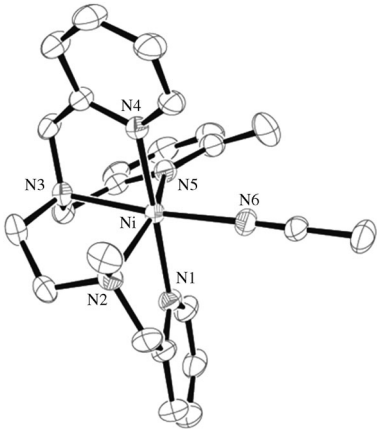

Figure 1. ORTEP diagram of $[Ni(L3)(CH_3CN)](BPh_4)_2$ (**3**) showing 50% probability thermal ellipsoids and the labeling scheme for selected atoms. All the hydrogen atoms are omitted for clarity.

Table 1. Selected bond lengths and bond angles for complex **3**.

Bond lengths [Å]		
	Ni1–N1	2.141(2)
	Ni1–N2	2.138(2)
	Ni1–N3	2.099(2)
	Ni1–N4	2.098(2)
	Ni1–N5	2.143(2)
	Ni1–N6	2.064(2)
Bond angles [°]		
	N1-Ni1-N2	78.11(9)
	N1-Ni1-N3	101.37(9)
	N1-Ni1-N4	173.84(9)
	N1-Ni1-N5	88.48(9)
	N1-Ni1-N6	86.98(9)
	N2-Ni1-N3	83.88(9)
	N2-Ni1-N4	96.09(9)
	N2-Ni1-N5	154.17(9)
	N2-Ni1-N6	94.12(10)
	N3-Ni1-N4	79.86(9)
	N3-Ni1-N5	77.19(9)
	N3-Ni1-N6	170.77(9)
	N4-Ni1-N5	97.68(9)
	N4-Ni1-N6	91.43(9)
	N5-Ni1-N6	107.25(10)

other Ni–N bonds on account of sp hybridization of the acetonitrile nitrogen atom (see above). Among the two tertiary amine nitrogen donor atoms the $N3_{amine}$ nitrogen atom is coordinated more strongly than the $N2_{amine}$ nitrogen atom, as expected. The N-Ni-N (77.19(9)–107.25(10)°) and N-Ni-N (154.17(9)–173.84(9)°) bond angles deviate from the ideal octahedral angles of 90 and 180°, respectively, revealing the presence of significant distortion in the Ni^{II} coordination geometry.

Structures of nickel(II) complexes: density functional theory (DFT) calculations

A DFT study (by using the Gaussian 09 program[56]) has been performed to investigate the geometrical parameters of complexes **1**, **3**, and **5** and the optimized geometries of them are provided in Figures S4, S6, and S7 in the Supporting Information. Initially, as a bench mark calculation, the crystal structure of complex **3** was optimized. The computed geometry is in good agreement with the experimentally determined crystal structure, except slight elongations in the bond lengths ranging from 0.04 to 0.13 Å (Figure S6 in the Supporting Information). Hence, the same computational methodology has been followed for optimizing the geometries of the complexes **1** and **5**. As for complex **3**, the complexes **1** and **5** (see the Supporting Information for the optimized structures Figures S4 and S7) also exhibit distorted octahedral coordination geometry.

In complex **1**, the $Ni–N_{py}$ bond lengths (Ni–N1 2.13, Ni–N5 2.14 Å) are shorter than the $Ni–N_{amine}$ bond lengths (Ni–N2 2.20, Ni–N3 2.16 Å), as expected.[36–38,40] However, the $Ni–N_{py}$ bond (Ni–N4 2.20 Å) is equal in length to the Ni–N2 bond but shorter than the Ni–N3 bond. Upon replacing one of the pyridyl nitrogen atoms in complex **1** by a 6-methylpyridyl nitrogen atom to give complex **3**, the $Ni–N_{py}$ (Ni–N5 2.21 Å) bond is weakened due to steric hindrance of the 6-methyl group but no appreciable change in the other bond lengths is observed. Upon replacing one of the pyridyl nitrogen atoms in complex **1** by a imidazolyl nitrogen atom to give complex **5**, the $Ni–N_{im}$ (Ni–N5 2.12 Å) bond becomes stronger than the $Ni–N_{py}$ bonds with increase in spin density of the Ni, as expected ($pK_a(BH^+)$: ImH^+ 6.0, pyH^+, 5.2), and no appreciable changes are observed in other bonds.

Electronic spectral properties

The electronic spectral data of the nickel(II) complexes are summarized in Table 2 and the typical electronic absorption spectrum of complex **1** is shown in Figure 2. In a dichloromethane/acetonitrile (3:1 v/v) solvent mixture, all the complexes exhibit absorption bands in the range $\lambda = 520–535$ nm and also a broad split band ($\lambda = 877–921$, 800–817 nm). The highest energy band is assigned to a $^3A_{2g} \rightarrow {}^3T_{1g}(F)$ (ν_2) transition, whereas the band in the range $\lambda = 800–817$ nm is assigned to a $^3A_{2g} \rightarrow {}^3T_{2g}(F)$ (ν_1) transition in a nickel(II) ion located in an octahedral environment.[40,44] The lowest energy band with an intensity almost equal to that of the ν_1 band is assigned to the

Table 2. UV/Vis spectral (λ_{max} in [nm], ε in [$M^{-1}cm^{-1}$] in parenthesis) and electrochemical data[a] of Ni^{II} complexes **1**–**5** in a dichloromethane/acetonitrile solvent mixture (3:1 v/v) at 25.0 °C.

	$^3A_{2g} \rightarrow {}^3T_{1g}(P)$ (ν_3) calcd[a]	$^3A_{2g} \rightarrow {}^3T_{1g}(F)$ (ν_2)	$^3A_{2g} \rightarrow {}^3T_{2g}(F)$ (ν_1)	$^3A_{2g} \rightarrow {}^1E_{1g}(D)$	B'	β[b] [%]
1	335	525 (16)	807 (16)	877 (20)	781	28
2	340	533 (15)	817 (16)	921 (20)	762	30
3	339	530 (15)	808 (11)	890 (13)	743	31
4	342	534 (18)	814 (11)	920 (16)	742	31
5	341	532 (22)	800 (19)	882 (19)	703	35

[a,b] Calculated by solving the quadratic equation and by using B as 1080 cm^{-1}.

© 2014 Wiley-VCH Verlag GmbH & Co. KGaA, Weinheim

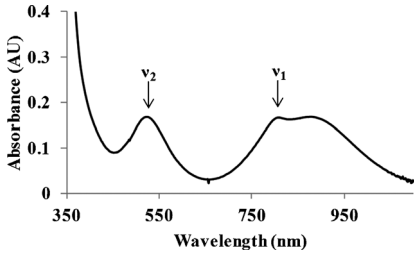

Figure 2. Electronic absorption spectrum of $[Ni(L3)(CH_3CN)](BPh_4)_2$ (1.0×10^{-2} M) in a dichloromethane/acetonitrile solvent mixture (3:1 v/v) at 25.0 °C.

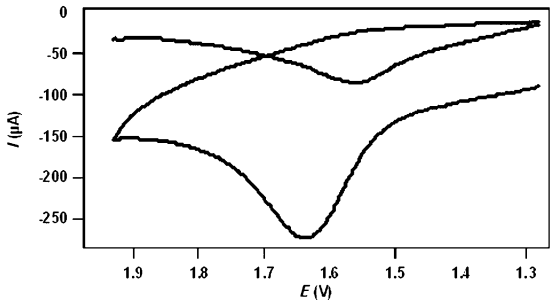

Figure 3. Cyclic voltammogram and differential pulse voltammogram of 1 mM complex $[Ni(L3)(ACN)]^{2+}$ in a dichloromethane/acetonitrile mixture at 25.0 °C. Supporting electrolyte: 0.1 M tetrabutylammonium perchlorate (TBAP), scan rate: 50 and 5 mV s^{-1} for CV for DPV, respectively.

$^3A_{2g}\rightarrow{}^1E_{1g}$(D) spin-forbidden transition. The ν_1 band for the present $[Ni(N5)(CH_3CN)]^{2+}$ complexes is observed at energies higher than those for the $[Ni(N4)(CH_3CN)_2]^{2+}$ complexes[40a] of related tetradentate ligands, which is expected due to the higher ligand field strength of N5 ligands with higher denticity. Similarly, the incorporation of a pyridylmethyl arm on the terminal tertiary amine nitrogen atom in $[Ni(iso\text{-}BPMEN)(CH_3CN)_2](BPh_4)_2$,[40a] where iso-BPMEN is *N*,*N*-dimethyl-*N*′,*N*′-bis(pyrid-2-ylmethyl)ethane-1,2-diamine, to obtain complex **1** the ligand field band is shifted from lower energy ($\lambda=842$ nm) to higher energy ($\lambda=807$ nm). The ν_1 band position depends on the donor atom type; thus, when the pyridylmethyl arm in complex **1** is replaced an imidazolylmethyl arm to obtain complex **5**, the ν_1 band is shifted to slightly higher energy because of the strongly σ-bonding imidazole donor atom (see above). On the other hand, the energy of the ν_1 band decreases when the pyridylmethyl arm in complex **1** is replaced by a 6-methylpyridyl arm to get complex **3**, and by a quinolylmethyl arm to get complex **4**, which is expected due to the weaker coordination of the sterically hindering 6-methylpyridyl (see above) and the quinolyl nitrogen donor atoms. Also, upon replacing the *N*-methyl group in complex **1** by a benzyl group to give complex **2** the band is shifted to lower energy ($\lambda=817$ nm) on account of the steric effect of the benzyl group. The observed ν_1 and ν_2 band positions were fitted into the quadratic equation[44] relating the energy of the ν_1 and ν_3 bands and the metal–ligand covalency parameter (β) calculated. The β values for the $[Ni(N5)(CH_3CN)]^{2+}$ complexes are higher, and the B' values calculated ($\tilde{\nu}=703$–781 cm^{-1}) are lower, than those ($\tilde{\nu}=773$–1038 cm^{-1}) for the $[Ni(N4)(CH_3CN)_2]^{2+}$ complexes,[40] which is expected.

Table 3. Electrochemical data[a] of nickel(II) complexes in dichloromethane/acetonitrile solution at 25.0 °C.

Complex	$E_{p,c}$ (CV) [V]	$E_{1/2}$ (DPV) [V]
$[Ni(L1)(CH_3CN)]^{2+}$	1.622	1.548
$[Ni(L2)(CH_3CN)]^{2+}$	1.628	1.554
$[Ni(L3)(CH_3CN)]^{2+}$	1.646	1.564
$[Ni(L4)(CH_3CN)]^{2+}$	1.690	1.584
$[Ni(L5)(CH_3CN)]^{2+}$	1.640	1.592

[a] Potential measured versus $Ag/AgNO_3$ (0.001 M, 0.1 M TBAP) in dichloromethane/acetonitrile solution; add 0.544 V to convert to standard hydrogen electrode (NHE).

Electrochemical properties

The electrochemical properties of the nickel(II) complexes were investigated in a dichloromethane/acetonitrile solvent mixture by employing cyclic (CV) and differential pulse voltammetry (DPV) on a stationary platinum electrode. All of the complexes show an anodic oxidation wave (1.622–1.690 V) but not any coupled reduction wave (Figure 3) corresponding to the Ni^{II}/Ni^{III} redox couple. The $E_{1/2}$ values of the redox couple (Table 3) fall in the range 1.548–1.592 V observed for a similar type of nickel(II) complexes[45] and follows the trend **1**<**2**<**3**<**4**<**5**. Upon replacing one of the pyridylmethyl arms in complex **1** by the imidazolyl nitrogen donor to give complex **5**, the redox potential ($E_{1/2}=1.592$ V) is shifted (44 mV) to a more positive value revealing that the strongly σ-bonding imidazolyl nitrogen atom (see above) renders the oxidation of Ni^{II} to Ni^{III} facile. Upon replacing the pyridylmethyl arm in complex **1** by the sterically hindering 6-methylpyridyl arm to give complex **3** or by the quinolylmethyl arm to give complex **4**, a positive shift in the redox potential ($E_{1/2}=20$ and 36 mV for complexes **3** and **4**, respectively) is observed suggesting that the oxidation of Ni^{II} is rendered facile. The sterically hindered 6-methylpyridyl (see above) and quinolylmethyl nitrogen donors are expected to increase the positive charge on the Ni^{II} center making the Ni^{II} to Ni^{III} oxidation difficult. However, the redox potential is shifted to more positive values revealing that the increase in the positive charge on nickel(II) is compensated by stronger coordination of the other nitrogen donors making the oxidation of Ni^{II} to Ni^{III} facile. A similar positive shift (6 mV) in $E_{1/2}$ is observed upon replacing the *N*-methyl group in complex **1** by the sterically hindering *N*-benzyl group to give complex **2**. Thus, changes in the Ni^{II}/Ni^{III} redox potential are observed upon varying the ligand donor functionalities.

Functionalization of alkanes

The catalytic ability of the complexes **1**–**5** towards oxidation of alkanes like cyclohexane, adamantane, and cumene was investigated by using *m*-CPBA, H_2O_2, and *t*BuOOH as oxidants in a di-

© 2014 Wiley-VCH Verlag GmbH & Co. KGaA, Weinheim

Table 4. Products of the oxidation of cyclohexane catalyzed[a] by the different Ni^{II} complexes.

	TON						
	Cyclohexanol	Cyclohexanone	ε-caprolactone	Total TON[b]	Chlorobenzene	A/K[c]	Yield[d] [%]
blank	3.0	1.0	–	4			
1	487	–	46	533	455	10.6	53.3
2	453	–	62	515	415	7.3	51.5
3	424	8	52	484	361	7.1	48.4
4	404	6	35	445	380	9.9	44.5
5	272	12	18	302	234	9.0	30.2

[a] Reaction conditions: catalyst (0.35×10^{-3} mmol dm^{-3}), substrate (2.45 mol dm^{-3}), oxidant (0.35 mol dm^{-3}) in a dichloromethane/acetonitrile solvent mixture (3:1 v/v). [b] Total TON = number of mmol of product/number of mmol of catalyst. The TON is the average of three determinations. [c] A/K = TON of cyclohexanol/(TON of cyclohexanone+TON of ε-caprolactone). [d] Yield based on the oxidant.

chloromethane/acetonitrile solvent mixture (3:1 v/v) at room temperature under an atmosphere of nitrogen and the results are summarized in Tables 4–6. When the catalytic activity of the Ni^{II} complexes was studied under air, the total TON for the cyclohexane oxidation is lower than that under a nitrogen atmosphere. It is probable that the $[(L)Ni^{II}–O^{\bullet}]$ radical intermediate generated during the catalytic cycle (see below) is quenched by dioxygen/moisture in air to give hydroxonickel species after some turnovers thereby decreasing the yield. The conversion of alkanes into hydroxylated products was quantified based on gas chromatographic analysis by using authentic samples and an internal standard. When H_2O_2/*t*BuOOH was used as the oxidant only trace amounts of the oxidized products were discerned (results are not shown here) revealing that the nickel(II) complexes are not effective as catalysts for these oxidants. It has been reported[46] that *m*-CPBA is a strong oxidizing agent for the oxidation of cyclohexane and adamantane to the corresponding alcohols and ketones in the absence of a metal catalyst but only under vigorous reaction conditions like very high concentration of *m*-CPBA, a long reaction time, and a high temperature. Thus, control reactions performed in the absence of complexes with *m*-CPBA as oxidant yielded only very small amounts of the oxidized products (TON(cyclohexane) = 4, TON(adamantane) = 9, TON(cumene) = 5) revealing that all the complexes act as catalysts towards the oxidation of alkanes. In the presence of complexes oxidation of cyclohexane takes place efficiently with 300–535 total TON with cyclohexanol (A) as the major product (TON = 272–487) and cyclohexanone (K; TON = 6–12), and ε-caprolactone (TON = 18–62) as the minor products the alcohol/ketone selectivity (A/K = 7.1–10.6) being appreciably good. The product ε-caprolactone is obtained by the over oxidation of cyclohexanone in the presence of an excess or unreacted *m*-CPBA. As *m*-CPBA is a reagent for the quantitative conversion of cyclic ketones to the corresponding lactones (Bayer–Villiger oxidation) in the absence of a metal catalyst, obviously ε-caprolactone is obtained not by metal-catalyzed oxidation. Also, the complexes catalyze the selective oxidation of adamantane to give a total TON of 600 with good to high 3°/2° regioselectivity of 11.5. Further, they selectively oxidize cumene to 2-phenyl-2-propanol with a total TON of 475.

Complex **1** catalyzes the oxidation of cyclohexane to give a total TON of 533 (TON(A) = 487, TON(K) = 12, A/K = 10.6) corresponding to 53% conversion of the oxidant to organic products. The total TON observed for complex **1** with an N5 ligand is lower than those for $[Ni(TPA)(OAc)(OH_2)]BPh_4$,[36] and $[Ni(iso\text{-}BPMEN)(CH_3CN)_2](BPh_4)_2$,[40a] where TPA and iso-BPMEN are tetradentate N4 ligands. There is only one easily replaceable monodentate ligand in complex **1**, whereas there are two such ligands in the complexes of the N4 ligands, leading to the enhancement in the catalytic activity. So, it is proposed that *m*-CPBA binds to the nickel(II) center in $[Ni(L1)(CH_3CN)]^{2+}$ by replacing the labile acetonitrile molecule to give the intermediate adduct species $[Ni^{II}(L1)(OOCOC_6H_4Cl)]^{+}$ (Scheme 2), which undergoes either 1) homolysis leading to the formation of $[(L1)Ni^{II}–O^{\bullet}]^{+}$/$[(L1)Ni^{III}{=}O]^{+}$ intermediate species (see below) and the *m*-chlorobenzoic acid radical or 2) heterolysis leading to the formation of the intermediate $[(L1)Ni^{IV}{=}O]^{2+}$ species and chlorobenzoic acid. The observation of chlorobenzene (75–85%) as product corresponding to the total TON supports the formation of the intermediate species $[(L1)Ni^{II}–O^{\bullet}]^{+}$/$[(L1)Ni^{III}{=}O]^{+}$ and reveals that the *m*-chlorobenzoate radical is

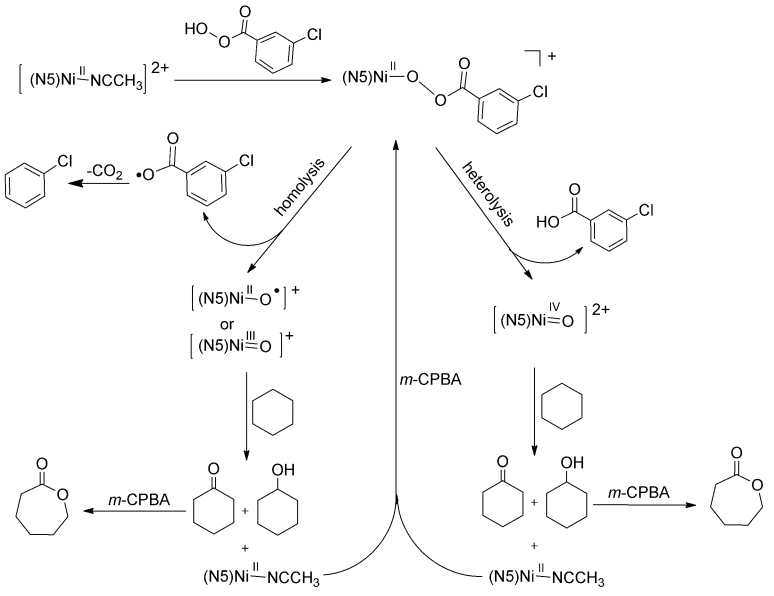

Scheme 2. Proposed mechanism of the alkane hydroxylation.

© 2014 Wiley-VCH Verlag GmbH & Co. KGaA, Weinheim

not the reactive intermediate as it readily undergoes decarboxylation rather than hydrogen abstraction from the alkane. This is consistent with the formation of remaining (15–25%) alkane hydroxylated products, which reveals that the gate for the formation of another intermediate species, possibly $[(N5)Ni^{IV}{=}O]^{2+}$, is unlocked. DFT studies (see below) also support the formation of the intermediate $[(L1)Ni^{II}{-}O^{\bullet}]^{+}$ species. Itoh et al. have proposed[37] the formation of adducts with *m*-CPBA, similar to $[Ni^{II}(L1)(OOCOC_6H_4Cl)]^{+}$, and reactive intermediates, to illustrate the catalytic activity of complexes of the type [Ni(L)(X)(X′)], where L is a tetradentate ligand and X as well as X′ are OAc^{-}, NO_3^{-}, *m*-chlorobenzoic acid (*m*-CBA), or phenolate. We have also successfully illustrated the trends in the catalytic activity of nickel(II) complexes of a series of N4 ligands[40a] towards alkane hydroxylation by invoking the formation of such an intermediate. The proposal of $[Ni^{II}(L1)(OOCOC_6H_4Cl)]^{+}$ as the intermediate adduct species is supported by the successful isolation and X-ray structure determination of the nickel(II) alkylperoxo complex $[Ni^{II}(Tp^{ipr})(OO\mathit{t}Bu)]$, which has been employed[39a] by Hikichi et al. for the oxidation of substituted alcohols to benzaldehydes. Also, Ray et al.[41] have used EPR and ESI-MS techniques to characterize the intermediate species $[(TMG_3tren)Ni{-}O(H)]^{n+}$, where TMG_3tren is tris(2-(*N*-tetramethylguanidyl)ethyl)amine and $n=1$ for oxo, $n=2$ for hydroxo, and proposed the involvement of $[(TMG_3tren)Ni^{III}{=}O(H)]$ intermediates in alkane hydroxylation reactions. Further, the formation of $[Ni^{IV}(O)(TMG_3tren)(OTf)]^{+}$ (OTf = triflate) in the reaction of $[Ni(TMG_3tren)(OTf)]OTf$ with *m*-CPBA[41] has been detected by using ESI-MS.

Upon replacing one of the pyridylmethyl arms in complex **1** by an imidazolylmethyl arm to give complex **5**, cyclohexane is catalytically oxidized with a total TON of 302 and a decrease in the alcohol selectivity (A/K = 9.0). The strongly σ-bonding imidazolyl nitrogen donor favors the formation of the reactive intermediate with a higher oxidation state (see above) so as to act as efficient catalysts for alkane hydroxylation. However, the lower π-bonding ability of the imidazolyl nitrogen atom does not facilitate stabilization of the reactive intermediate rendering complex **5** as a less efficient catalyst. Upon replacing the methyl group in complex **1** by a benzyl group to give complex **2**, both the total TON (515) and the A/K ratio (7.3) decrease. The introduction of the bulky *N*-benzyl moiety renders the coordination of the tertiary amine nitrogen atom to the Ni^{II} center weaker, which is revealed by the slightly higher Ni^{II}/Ni^{III} redox potential of complex **2** (see above) leading to stronger coordination of the other nitrogen atoms and a decrease in the stabilization of high-valent nickel-oxo species, and hence the lower catalytic activity of complex **2**. Molecular model building studies of complex **2** reveal that the unfavorable steric interactions occurring between the *N*-benzyl group and the pyridine ring renders the binding of *m*-CPBA difficult, contributing to the lower yield. This is supported by the observation that complex **3** (total TON = 484, A/K = 7.1) and complex **4** (total TON = 445, A/K = 9.9) act as less efficient catalysts towards cyclohexane oxidation; the sterically hindering 6-methyl group in complex **3** and the bulky quinolyl group in complex **4** decrease the tendency of the nitrogen atom of the pyridylmethyl and the quinolylmethyl arms to be involved in π-backbonding. All the above-described observations reveal that a π-accepting ligand donor like a pyridine/quinoline nitrogen atom stabilizes the high-valent nickel-oxo intermediate species leading to an enhanced catalytic activity towards oxidation of alkanes, whereas a strongly σ-bonding but weakly π-backbonding ligand donor like imidazole destabilizes it, leading to a decreased catalytic activity. Also, interestingly, the total TON for the cyclohexane oxidation reaction correlates linearly with the metal–ligand covalency parameter β (Figure 4) and also the Ni^{II}/Ni^{III} redox couple (Figure 5). A similar linear correlation between the total TON and β has been observed[40a] by us for

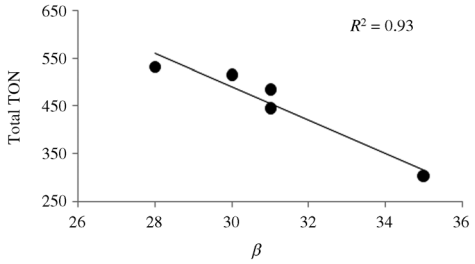

Figure 4. Correlation between the oxidation of cyclohexane and the β values at 25.0 °C. $R^2 = 0.93$.

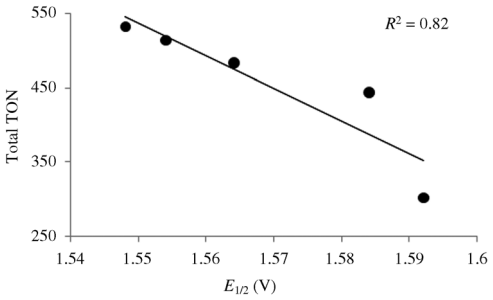

Figure 5. Correlation between the total TON for the cyclohexane oxidation and the Ni^{II}/Ni^{III} redox potential. $R^2 = 0.82$.

Ni(N4) complexes; an increase in the TON with an increase in β means that the total TON increases with an increase of the ability of the N4 ligands to get involved in π-backbonding and hence stabilize the reactive intermediate. However, for the present complexes the total TON decreases with an increase in the value of β and thus complex **5** with the imidazolyl nitrogen donor shows the highest value for β but the lowest TON. The catalytic ability of Ni(N5) complexes show lower catalytic ability than Ni(N4) complexes as the former complexes make available only a single coordination site for binding with the oxidant, whereas the latter complexes offer two binding sites. Also, as only a single coordination site is made available for the oxo group in the Ni^{II} complexes of N5 ligands, the π-backbonding of the oxo group with nickel is not facilitated.

© 2014 Wiley-VCH Verlag GmbH & Co. KGaA, Weinheim

Table 5. Products of the oxidation of adamantane catalyzed[a] by the different Ni^{II} complexes.

	TON					
	1-Adamantanol	2-Adamantanol	2-Adamantanone	Total TON[b]	3°/2°[c]	Yield[d] [%]
blank	6.2	2.4	0.4	9.0		
1	464	123	8	595	10.6	59.5
2	451	114	10	575	10.9	57.5
3	413	101	13	527	10.9	52.7
4	458	109	11	578	11.5	57.8
5	402	102	8	512	11.0	51.2

[a] Reaction conditions: catalyst (0.2×10^{-3} mmol dm^{-3}), substrate (0.4 mol dm^{-3}), oxidant (0.2 mol dm^{-3}) in a dichloromethane/acetonitrile solvent mixture (3:1 v/v). [b] TON = number of mmol of product/number of mmol of catalyst. The TON is the average of three determinations. [c] 3°/2° = (TON of 1-adamantanol × 3)/(TON of 2-adamantanol + TON of 2-adamantanone). [d] Yield based on the oxidant.

Table 6. Oxidation product of the oxidation of cumene catalyzed[a] by the different Ni^{II} complexes.

Complex	2-phenyl-2-propanol	Total TON[b]	Yield[c] [%]
blank	5	5	0.5
1	475	475	47.5
2	460	460	46.0
3	418	418	41.8
4	441	441	44.1
5	327	327	32.7

[a] Reaction conditions: catalyst (0.35×10^{-3} mmol dm^{-3}), substrate (2.45 mol dm^{-3}), oxidant (0.35 mol dm^{-3}) in a dichloromethane/acetonitrile solvent mixture (3:1 v/v). [b] Total TON = number of mmol of product/number of mmol of catalyst. The TON is the average of three determinations. [c] Yield based on the oxidant.

Adamantane and cumene oxidation

The catalytic activity of complexes **1**–**5** towards the oxidation of adamantane has been also explored and the results are summarized in Table 5. Adamantane is efficiently oxidized to give 1-adamantanol and 2-adamantanol as the major products along with a small amount of 2-adamantanone as the minor product. Complex **1** catalyzes the oxidation of adamantane to give a total TON 595 with a high 3°/2° bond selectivity (10.6). The replacement of the methyl substituent in complex **1** by the *N*-benzyl substituent to give complex **2** leads to a decrease in the total TON (575) but with a slight increase in the 3°/2° bond selectivity (10.9). Upon replacing the pyridylmethyl arm in complex **1** by the 6-methylpyridylmethyl arm as in complex **3** (TON = 527, 3°/2° = 10.9) or the quinolylmethyl arm as in complex **4** (TON = 578, 3°/2° = 11.5) or the imidazolylmethyl arm as in complex **5** (TON = 512, 3°/2° = 11.0) the total TON decreases with the 3°/2° bond selectivity remaining almost the same. This trend in the catalytic activity is similar to that observed for the cyclohexane oxidation revealing the involvement of the same type of high-valent nickel-oxo intermediate species in the adamantane oxidation. A good π-backbonding pyridine donor facilitates the formation of the high-valent nickel-oxo species, whereas a strongly σ-donating imidazole nitrogen atom destabilizes it but slightly increases the 3°/2° bond selectivity. However, the total TON does not correlate well with the $E_{1/2}$ or β values (Figures S1 and S2 in the Supporting Information). The catalytic activity of the Ni^{II} complexes towards the oxidation of cumene has also been investigated and the results are summarized in Table 6. Interestingly, all the complexes catalyze the oxidation of cumene selectively to form 2-phenyl-2-propanol without any side product, and a linear correlation between the TON and the β values has been observed (Figure S3 in the Supporting Information), illustrating the importance of the π-backbonding of the heterocyclic nitrogen donor atom.

Proposed mechanism for $[(L1/L5)Ni^{II}–O^{\bullet}]^{+}$-catalyzed cyclohexane oxidation

As shown in Scheme 2, the Ni^{II}-catalyzed alkane oxidation involves: 1) *m*-CPBA binding to Ni^{II} by replacing a CH_3CN molecule, 2) homolytic or heterolytic O–O bond cleavage of *m*-CPBA to generate the $Ni^{II}–O^{\bullet}$ or $Ni^{IV}=O$ intermediate, and 3) oxidation of the alkane by the intermediate. For the computational investigation of the mechanism of catalysis, Ni^{II} complexes of L1 and L5 were considered as they show a large difference in the yield of the product (Table 4). It should be noted that so far no detailed study on the mechanism of a nickel(II)-mediated alkane oxidation has been attempted and many DFT methods have been used in the present study to locate the ground-state configuration of the reactive intermediate. Previously, Comba et al. investigated the $Fe^{IV}(O)$- or $Fe^{V}(O)$-catalyzed cyclohexane oxidation by using similar DFT methods.[47] The energetics computed for $Ni^{IV}=O$ and $Ni^{II}–O^{\bullet}$ species in their different spin levels (B3LYP/B2 method) show that the $Ni^{IV}=O$ intermediate is significantly destabilized by more than 900 kJ mol^{-1} compared to the corresponding $Ni^{II}–O^{\bullet}$ species (see Table S1 in the Supporting Information). These results strongly support the homolytic O–O bond cleavage pathway and involvement of $Ni^{III}=O/Ni^{II}–O^{\bullet}$ species in the reaction proposed above (Scheme 2), ruling out the formation of the $Ni^{IV}=O$ intermediate. Also, all attempts to optimize $[(L1)Ni^{III}=O]^{+}$ and $[(L5)Ni^{III}=O]^{+}$ in the high-spin state ($S = 3/2$) only led to the formation of the high-spin $Ni^{II}–O^{\bullet}$ species $\mathbf{1}\,\mathbf{b}_{hs}$ ($\rho_{(Ni)} = 1.56$, $\rho_{(O1)} = 1.16$) and $\mathbf{5}\,\mathbf{b}_{hs}$ ($\rho_{(Ni)} = 1.57$, $\rho_{(O1)} = 1.16$), respectively (Figures 6 and 7). The $\rho_{(Ni)}$ and $\rho_{(O1)}$ values of $\mathbf{1}\,\mathbf{b}_{hs}$ and $\mathbf{5}\,\mathbf{b}_{hs}$ indicate the presence of two unpaired electrons on the Ni and one unpaired electron on the O1, which are ferromagnetically coupled. The computed singly occupied molecular orbitals (SOMOs) of $\mathbf{1}\,\mathbf{b}_{hs}$ and $\mathbf{5}\,\mathbf{b}_{hs}$ (Figure 8) indicate that one of the two unpaired electrons of the Ni resides in a non-bonded $d_{x^2-y^2}$ orbital, whereas the other one resides in a $\sigma^*d_{z^2}–p_z$ orbital (with respect to the Ni–O1 interaction), and the unpaired electron on the O1 is located in a $\pi^*d_{yz}–p_y$ orbital. The low-spin ($S = 1/2$) intermediate $[(L1/L5)Ni^{II}–O^{\bullet}]^{+}$ species $\mathbf{1}\,\mathbf{b}_{ls}$ ($\rho_{(Ni)} = 1.56$, $\rho_{(O1)} = -0.83$) and $\mathbf{5}\,\mathbf{b}_{ls}$ ($\rho_{(Ni)} = 1.58$, $\rho_{(O1)} = -0.82$) have also been modeled and they are found to be less stable than $\mathbf{1}\,\mathbf{b}_{hs}$ and $\mathbf{5}\,\mathbf{b}_{hs}$ by +25.1 and +16.2 kJ mol^{-1}, respectively (Figures 6 and 7). In addition, the

© 2014 Wiley-VCH Verlag GmbH & Co. KGaA, Weinheim

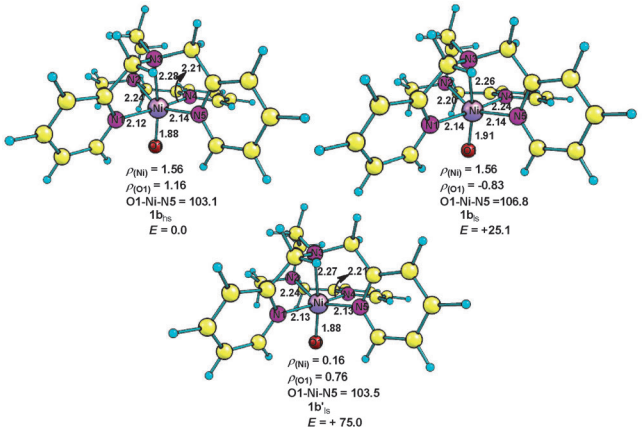

Figure 6. Optimized geometries of $[(L1)Ni^{II}–O^{\bullet}]^{+}$ (**1 b**) in their high-spin ($S=3/2$) and low-spin ($S=1/2$) states along with the low-spin $[(L1)Ni^{III}=O]^{+}$ species. Energies in [kJ mol^{-1}], bond lengths in [Å], and angles in [°].

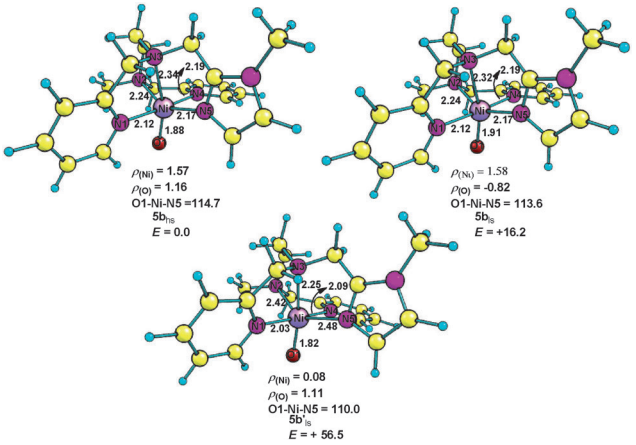

Figure 7. Optimized geometries of $[(L5)Ni^{II}–O^{\bullet}]^{+}$ (**5 b**) in their high-spin ($S=3/2$) and low-spin ($S=1/2$) states along with the low-spin $[(L5)Ni^{III}=O]^{+}$ species. Energies in [kJ mol^{-1}], bond lengths in [Å], and angles in [°].

low-spin ($S=1/2$) intermediate $[(L1/L5)Ni^{III}=O]^{+}$ species $\mathbf{1b'_{ls}}$ ($\rho_{(Ni)}=0.16$, $\rho_{(O1)}=0.76$), and $\mathbf{5b'_{ls}}$ ($\rho_{(Ni)}=0.08$, $\rho_{(O1)}=1.11$) with one unpaired electron on the nickel have been computed and they are less stable than $\mathbf{1b_{hs}}$ and $\mathbf{5b_{hs}}$ by +75.0 and +56.5 kJ mol^{-1} respectively, and so they are discarded from mechanistic investigation.

For the mechanistic investigation on the alkane oxidation step, both high- and low-spin $[(L1)Ni^{II}–O^{\bullet}]^{+}$ and $[(L5)Ni^{II}–O^{\bullet}]^{+}$ species have been considered as they are the species most likely formed in the homolytic pathway (Scheme 2). We now propose a mechanism for the Ni^{II}–$O^{\bullet}$-catalyzed cyclohexane oxidation (Scheme 3), which is similar to the one proposed by Comba et al.[47] for the $Fe^{IV}=O/Fe^{V}=O$-catalyzed mechanism based on DFT

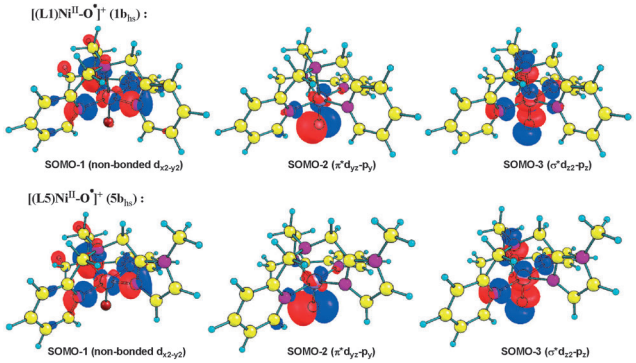

Figure 8. Singly occupied molecular orbitals for $\mathbf{1b_{hs}}$ and $\mathbf{5b_{hs}}$. Molecular orbitals are named based on the Ni–O1 interactions. The *x*, *y*, and *z* axes point along the Ni–N5, Ni–N4, and Ni–N3 directions, respectively (atom numbering is similar to the optimized geometries in Figures 6 and 7).

methods. It involves initial hydrogen abstraction by the Ni^{II}–$O^{\bullet}$ species (ts1) leading to the formation of Ni^{II}–OH and the cyclohexyl radical (rad_{int}), which reacts over through the C–O rebound step (ts2) to form the cyclohexanol product coordinated to the Ni^{I} species.

Relative stabilities of high-spin and low-spin intermediate $[(L1/L5)Ni^{II}$-$O^{\bullet}]^{+}$ species

Initially, the reliability of the B3LYP/B1 method was tested by optimizing the coordination geometry of $[Ni(L3)(CH_3CN)]^{2+}$ (**3**) (Figure S4 in the Supporting Information), which reproduces the X-ray crystal structure well, except slight elongations in the Ni–N bond lengths (0.05 to 0.10 Å). The spin density on the Ni center ($\rho_{(Ni)}$) is 1.58 with the remaining spins delocalized on the nitrogen atom, which confirms the presence of two unpaired electrons on the Ni^{II} in complex **3**. As the spin densities ($\rho_{(Ni)}$) of $\mathbf{1b_{hs}}$ and $\mathbf{5b_{hs}}$ are almost equal to that of Ni^{II} in complex **3**, it is clear that both $\mathbf{1b_{hs}}$ and $\mathbf{5b_{hs}}$ are high-spin $[(L1/L5)Ni^{II}–O^{\bullet}]^{+}$ species. As mentioned above, the high-spin states $\mathbf{1b_{hs}}$ and $\mathbf{5b_{hs}}$ are more stable than the corresponding low-spin species. In order to verify that this energy preference of the high-spin state is not an artifact of the level of theory used, a benchmark study was conducted by using six other DFT methods, namely, B3LYP-D, wB97XD, B97D, M06-2X, B3LYP*, and B3LYP** along with single-point calculations by using the TPSSh and OLYP methods (Table 7).[48,59] All the methods consistently show the high-spin state as the ground states for both **1 b** and **5 b**. In the case of **1 b**, the low-spin states $\mathbf{1b_{ls}}$ and $\mathbf{1b'_{ls}}$ are destabilized by +15.0 and +75.0 kJ mol^{-1}, respectively, relative to

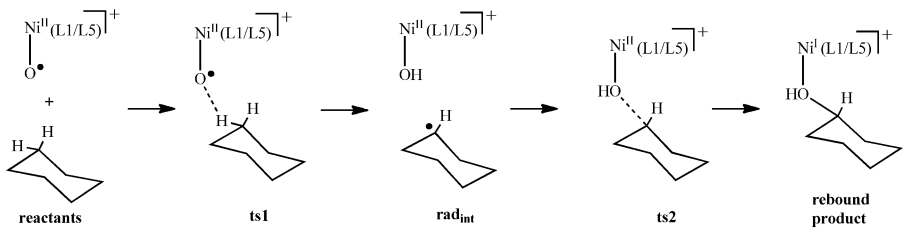

Scheme 3. Proposed mechanism for the $[(L1/L5)Ni^{II}–O^{\bullet}]^{+}$-catalyzed cyclohexane oxidation/hydroxylation.

© 2014 Wiley-VCH Verlag GmbH & Co. KGaA, Weinheim

Table 7. Relative free energies in [kJ mol^{-1}] of [(L1/L5)Ni^{II}–O$^{\bullet}$]$^{+}$ species with different DFT methods in their high-spin ($S=3/2$) and low-spin ($S=1/2$) states. The columns **1b**$'_{ls}$ and **5b**$'_{ls}$ show the [(L1/L5)Ni^{III}=O]$^{+}$ with low-spin ($S=1/2$) state.

Methods[a]	[(L1)Ni^{II}-O$^{\bullet}$]$^{+}$			[(L5)Ni^{II}-O$^{\bullet}$]$^{+}$		
	1b$_{hs}$ ($S=3/2$)	**1b**$_{ls}$ ($S=3/2$)	**1b**$'_{ls}$ ($S=3/2$)	**5b**$_{hs}$ ($S=3/2$)	**5b**$_{ls}$ ($S=3/2$)	**5b**$'_{ls}$ ($S=3/2$)
B3LYP	+0.0	+25.8	+74.8	+0.0	+18.1	+50.9
B3LYP-D	+0.0	+17.4	+74.6	+0.0	+16.9	+57.8
wB97XD	+0.0	+15.8	+72.9	+0.0	+14.8	–[b]
M06–2X	+0.0	+14.9	+53.1	+0.0	+13.6	+60.2
B3LYP*	+0.0	+16.3	+63.1	+0.0	+17.8	+39.5
B3LYP-D//OLYP	+0.0	+36.5	+61.6	+0.0	+34.3	+38.3
B3LYP-D//TPSSh	+0.0	+18.9	+77.4	+0.0	+19.4	+58.4

[a] For all methods the B1 basis sets were employed, optimization with other DFT methods such as BP86, B3LYP** were failed to produce all three intermediates. [b] Reproduces the **5b**$_{ls}$ spin state.

the high-spin state **1b**$_{hs}$. Similarly, the low-spin states **5b**$_{ls}$ and **5b**$'_{ls}$ are +14.0 and +54.0 kJ mol^{-1}, respectively, less stable than the high-spin state **5b**$_{hs}$. For both **1b** and **5b**, the spin density distribution at the Ni and O1 atoms are very similar to those described at the B3LYP/B1 level. Overall, all the six methods show that the high-spin [(L1/L5)Ni^{II}–O$^{\bullet}$]$^{+}$ species is the ground state. Due to the consistently lower energy gaps observed for **1b**$_{hs}$–**1b**$_{ls}$ and **5b**$_{hs}$–**5b**$_{ls}$, both the **1b**$_{hs}$ and **5b**$_{hs}$ species are selected for mechanistic studies.

In order to further verify the reliability of the B3LYP/B1 method to compute the geometries and reactivities of the Ni^{II} complexes, we have optimized the intermediate hydroxo [Ni^{III}-(TMG$_3$tren)(OH)]$^{2+}$ as well as the oxo [Ni^{III}(TMG$_3$tren)(O)]$^{+}$ species, which were spectroscopically characterized by Ray et al.[41] in both the high-spin ($S=3/2$) and the low-spin ($S=1/2$) state. We found that the low-spin state of [Ni^{III}(TMG$_3$tren)(OH)]$^{2+}$ is more stable than the corresponding high-spin state by +19.8 kJ mol^{-1} (Figure S5 in the Supporting Information), which is in agreement with the experimental findings. On the other hand, only the high-spin state of [Ni^{III}(TMG$_3$tren)(O)]$^{+}$ is located as the minimum and all attempts to optimize the low-spin state of [Ni^{III}(TMG$_3$tren)(O)]$^{+}$ were fruitless. Although a direct comparison of the present N5-ligand-coordinated [(L1/L5)Ni^{II}–O$^{\bullet}$]$^{+}$ species with the intermediate species of Ray et al. is difficult, it is interesting to see that only a terminal Ni^{III}–OH bond is present in the low-spin ground state of [Ni^{III}-(TMG$_3$tren)(OH)]$^{2+}$, whereas only a terminal Ni^{III}–O bond is present in the high-spin ground state of [(L1/L5)Ni^{II}–O$^{\bullet}$]$^{+}$.

Computed mechanism of the [(L1/L5)Ni^{II}–O$^{\bullet}$]$^{+}$-catalyzed cyclohexane hydroxylation

The computed free energy profile at the B3LYP/B2//B3LYP/B1 level of the two reaction steps, passing through the transition states ts1 and ts2 (Scheme 3) relative to the infinitely separated [(L1)Ni^{II}–O$^{\bullet}$]$^{+}$ (**1b**$_{hs}$) and cyclohexane is shown in Figure 9. In the first step, one of the equatorial hydrogen atoms of cyclohexane is abstracted by the terminal oxygen atom of **1b**$_{hs}$,

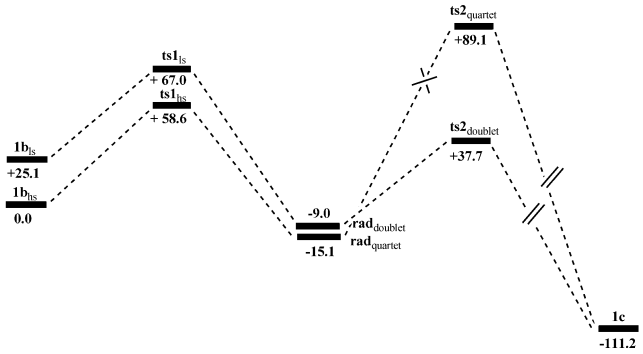

Figure 9. Computed free energy profile (B3LYP/B2//B3LYP/B1 level) for the [(L1)Ni^{II}–O$^{\bullet}$]$^{+}$ (**1b**)-catalyzed cyclohexane oxidation. Energies in [kJ mol^{-1}].

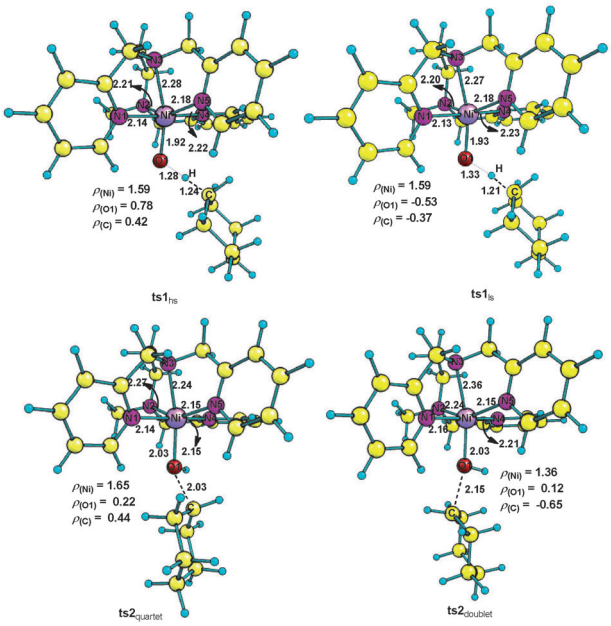

Figure 10. Computed geometries of the transition states along with the key spin densities for [(L1)Ni^{II}–O$^{\bullet}$]$^{+}$ (**1b**$_{hs}$)-catalyzed cyclohexane hydroxylation. Bond lengths in [Å].

which leads to the formation of [(L1)Ni^{II}(OH)]$^{+}$ and a cyclohexyl radical (rad$_{int}$). This step is associated with the transition state ts1$_{hs}$ (Figure 10, $E=+58.6$ kJ mol^{-1}), with C–H and O1–H bond lengths of 1.24 and 1.28 Å, respectively, and the Ni–O1 bond being elongated by 0.04 Å (vs. 1b$_{hs}$). The spin density of the Ni, O1, and C centers of ts1$_{hs}$ ($\rho_{(Ni)}=1.59$, $\rho_{(O1)}=0.78$, $\rho_{(C)}=0.42$) indicate the formation of a terminal O–H bond and the cyclohexyl radical. Subsequently, ts1$_{hs}$ decays into rad$_{quartet}$ ($E=-15.1$ kJ mol^{-1}, $\rho_{(Ni)}=1.6$, $\rho_{(O1)}=0.15$, $\rho_{(C)}=0.98$), in which the unpaired electron of the cyclohexyl carbon atom couples ferromagnetically with the unpaired electrons of Ni^{II} in **1b**$_{hs}$ (see Figure S6 in the Supporting Information for the optimized structures). As for ts1$_{hs}$, the ts1$_{ls}$ ($E=+67.0$ kJ mol^{-1}, $\rho_{(Ni)}=1.59$, $\rho_{(O1)}=-0.53$, $\rho_{(C)}=-0.37$) has been also computed and is found to be slightly uphill (by +8.3 kJ mol^{-1}) compared to ts1$_{hs}$. It then leads to the generation of rad$_{doublet}$ ($E=-9.0$ kJ mol^{-1}, $\rho_{(Ni)}=1.60$, $\rho_{(O1)}=0.13$, $\rho_{(C)}=-0.98$) in which the

© 2014 Wiley-VCH Verlag GmbH & Co. KGaA, Weinheim

cyclohexyl radical is antiferromagnetically coupled with the unpaired electrons of the Ni^{II}. Interestingly, the computed intermediates $rad_{quartet}$ and $rad_{doublet}$ are very close in energy (−15.1 and −9.0 kJ mol^{-1}, respectively), which was verified by optimizing the intermediates with the B3LYP*/B1 method and $rad_{quartet}$ is more stable than $rad_{doublet}$ by only +3.9 kJ mol^{-1}.

In the next step, the radical carbon atom approaches the Ni^{II}–OH species, which is modeled by varying the C–O bond length. The transition states for this step are found at quartet and doublet surfaces as $ts2_{quartet}$ (E = +89.1 kJ mol^{-1}, $\rho_{(Ni)}$ = 1.65, $\rho_{(O1)}$ = 0.22, $\rho_{(C)}$ = 0.44) and $ts2_{doublet}$ (E = +37.7 kJ mol^{-1}, $\rho_{(Ni)}$ = 1.36, $\rho_{(O1)}$ = 0.12, $\rho_{(C)}$ = −0.65), respectively. The transition state $ts2_{quartet}$ is associated with an activation energy of +89.1 kJ mol^{-1}, which is +30.5 kJ mol^{-1} higher than $ts1_{hs}$ for hydrogen abstraction. In contrast, the $ts2_{doublet}$ is associated with an activation energy, which is +20.9 kJ mol^{-1} lower than $ts1_{hs}$ and +29.2 kJ mol^{-1} lower than $ts1_{ls}$. Thus, it is evident that, as the $rad_{quartet}$ and $rad_{doublet}$ states are very close in energy and are thermodynamically very stable, they will easily interchange with one another[47,48] through spin flipping and the reaction pathway follows the low-energy barrier route involving $ts2_{doublet}$ rather than the one involving the higher energy transition state $ts2_{quartet}$. The spin-state analysis of the transition states reveal that both will end up to give the same rebound product in which Ni^{II} is reduced to Ni^{I}, which is confirmed by modeling the rebound product (**1c**, E = −111.2 kJ mol^{-1}, $\rho_{(Ni)}$ = 0.94).

The computed free-energy profile for $[(L5)Ni^{II}–O^{\bullet}]^{+}$ (**5b**)-catalyzed cyclohexane hydroxylation is shown in Figure 11 and the energetics are quoted relative to the free intermediate $\mathbf{5b}_{hs}$ species plus the cyclohexane molecule. The optimized intermediates associated with this pathway are shown in Figure S7 in the Supporting Information and the transition-state geometries are shown in Figure 12. In the case of **5b**, the hydrogen-abstraction step proceeds through the transition states $ts1_{hs}$ (E = +52.0 kJ mol^{-1}, $\rho_{(Ni)}$ = 1.59, $\rho_{(O1)}$ = 0.79, $\rho_{(C)}$ = 0.42) and $ts1_{ls}$ (E = +60.8 kJ mol^{-1}, $\rho_{(Ni)}$ = 1.60, $\rho_{(O1)}$ = −0.53, $\rho_{(C)}$ = −0.36). As found for **1b**, the $ts1_{ls}$ for **5b** is found to be slightly higher in energy than $ts1_{hs}$ by +8.9 kJ mol^{-1}. Here again, the hydrogen abstraction leads to the formation of the more degenerate

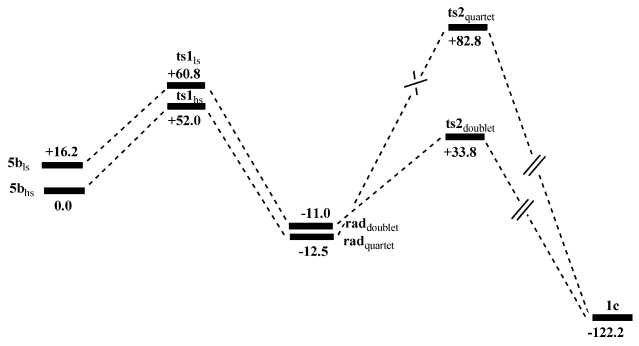

Figure 11. Computed free energy profile (B3LYP/B2//B3LYP/B1 level) for the $[(L5)Ni^{II}–O^{\bullet}]^{+}$ (**5b**)-catalyzed cyclohexane oxidation. Energies in [kJ mol^{-1}].

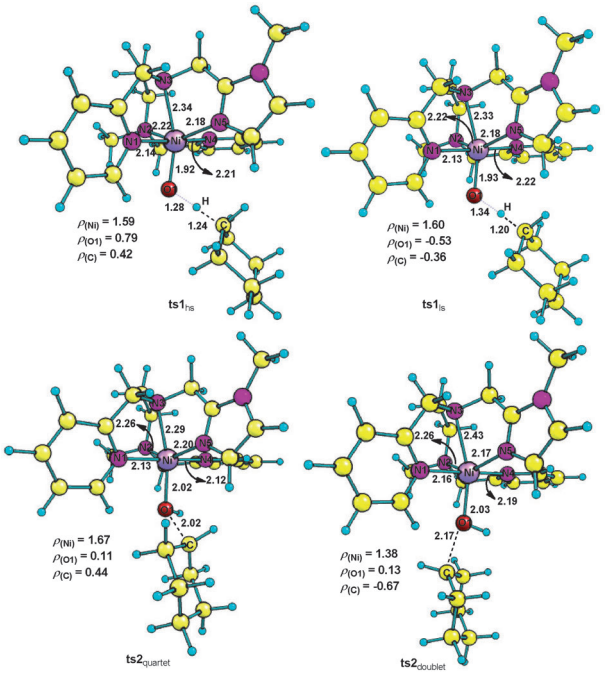

Figure 12. Computed geometries of the transition states along with the key spin densities for $[(L5)Ni^{II}–O^{\bullet}]^{+}$ ($\mathbf{5b}_{hs}$)-catalyzed cyclohexane hydroxylation. Bond lengths in [Å].

$rad_{quartet}$ (E = −12.5 kJ mol^{-1}, $\rho_{(Ni)}$ = 1.62, $\rho_{(O1)}$ = 0.16, $\rho_{(C)}$ = 0.98) and $rad_{doublet}$ (E = −11.0 kJ mol^{-1}, $\rho_{(Ni)}$ = 1.61, $\rho_{(O1)}$ = 0.23, $\rho_{(C)}$ = −0.98) intermediates, which indicates the occurrence of facile spin flipping between the $rad_{quartet}$ and $rad_{doublet}$ species. As for **1b**, the C–O rebound step for **5b** also pursues a trend similar to **1b** in such a way that the activation energy barrier of $ts2_{quartet}$ (E = +82.8 kJ mol^{-1}) is higher than that of $ts2_{doublet}$ (E = +33.8 kJ mol^{-1}). Both the ts2 states will lead to the formation of Ni^{I}-rebound product with overall reaction energy of −122.2 kJ mol^{-1}.

Overall, the computed energetics given in Figures 9 and 11 lead to the following mechanistic details: 1) the ground-state configuration of the active species is in a high-spin state ($\mathbf{1b}_{hs}$ or $\mathbf{5b}_{hs}$) and will pass through a hydrogen-abstraction transition state ($ts1_{hs}$) to yield a more stable radical intermediate $rad_{quartet}$, which is in equilibrium with $rad_{doublet}$ by readily undergo spin flipping; 2) in the C–O rebound step, $rad_{doublet}$ follows the low-energy pathway involving the $ts2_{doublet}$ to yield the product. Thus, it is interpreted that the reaction preferably goes through high-spin $\mathbf{ts1}_{hs}$ for hydrogen abstraction and low-spin $ts2_{doublet}$ for a C–O rebound step, that is, a two spin state reactivity; 3) for both **1b** and **5b**, a minor pathway through the low-spin transition state ($ts1_{ls}$) is also possibly operating along with the above-described major pathway occurring through the high-spin transition state $ts1_{hs}$, as both $\mathbf{1b}_{hs}$ and $\mathbf{5b}_{hs}$ may coexist due to a small energy gap for the spin cross over; 4) overall a two spin-state reactivity is predicted for the $[(L1/L5)Ni^{II}–O^{\bullet}]^{+}$-catalyzed cyclohexane hydroxylation reaction wherein the rate-determining step is the hydrogen abstraction.

© 2014 Wiley-VCH Verlag GmbH & Co. KGaA, Weinheim

Comparison of the reaction pathways modeled for $[(L1)Ni^{II}–O^{\bullet}]^{+}$ (1b) and $[(L5)Ni^{II}–O^{\bullet}]^{+}$ (5b)

The reaction pathways modeled for the **1b**- and **5b**-catalyzed cyclohexane hydroxylation are essentially the same. However, a comparison of the energetics of ts1 in the high-spin ($S=3/2$) and low-spin ($S=1/2$) states for **1b** and **5b** reveals that the $ts1_{hs}$ and $ts1_{ls}$ of **1b** have activation energies slightly higher ($\approx +6.0$ kJ mol^{-1}) than those of **5b**, which means that the catalytic efficiency of **1b** is less than that of **5b**. However, on the basis of the computational method used in this study and the data obtained, the expected error limit is $\pm$(10.0–15.0) kJ mol^{-1}.[49] So, it is evident that both **1b** and **5b** can be considered to have almost the same activation energy barriers and hence would compete with each other to be equally efficient towards cyclohexane hydroxylation. However, it should be noted that **1b** produces cyclohexanol (53.3%) in higher amount than **5b** (30.2%). To throw light on the higher catalytic activity of **1b** and to get further mechanic insights, the homolytic O–O bond cleavage of $[Ni^{II}(L1/L5)(OOCOC_6H_4Cl)]^{+}$ (**1a/5a**) to obtain $[(L1/L5)Ni^{II}–O^{\bullet}]^{+}$ (**1b/5b**) along with the *m*-CPBA radical (Scheme 2), has been modeled. It was found that the reaction energy ($\Delta E_{R.E}$) for the formation of $\mathbf{1b}_{hs}$ is $+99.3$ kJ mol^{-1}, which is $+8.4$ kJ mol^{-1} lower than that for $\mathbf{5b}_{hs}$ ($\Delta E_{R.E}=+107.7$ kJ mol^{-1}), and this means that the $\mathbf{1b}_{hs}$ species $[(L1)Ni^{II}–O^{\bullet}]^{+}$ is thermodynamically more easily accessible than the $\mathbf{5b}_{hs}$ species $[(L5)Ni^{II}–O^{\bullet}]^{+}$ from **1a** and **5a**, respectively. It is evident that π-backbonding by the pyridine nitrogen atom stabilizes the high-valent intermediate $[(L1)Ni^{II}–O^{\bullet}]^{+}$ ($\mathbf{1b}_{hs}$) species, whereas σ-donation by the imidazole nitrogen atom destabilizes the $[(L5)Ni^{II}–O^{\bullet}]^{+}$ ($\mathbf{5b}_{hs}$) species. The thermodynamically more stable $\mathbf{1b}_{hs}$ is expected to stabilize the associated $ts1_{hs}$ species, and hence with the inclusion of formation energy of $\mathbf{1b}_{hs}$, $ts1_{hs}$ has an activation energy barrier slightly lower ($\approx +2.0$ kJ mol^{-1}) than that of $\mathbf{5b}_{hs}$. This trend is consistent with the experimentally observed higher catalytic activity of $[Ni(L1)(CH_3CN)]^{2+}$ (**1**) than $[Ni(L1)(CH_3CN)]^{2+}$ (**5**). Thus, the homolytic O–O bond cleavage step plays a key role in determining the catalytic activity of **1** and **5** and so the catalytic activity mainly depends upon the thermodynamic stability of $\mathbf{1b}_{hs}$ and $\mathbf{5b}_{hs}$. However, it should be noted that the $\Delta E_{R.E}$ value for the formation of $\mathbf{1b}_{ls}$ ($\Delta E_{R.E}=+124.4$ kJ mol^{-1}) is almost the same as that for $\mathbf{5b}_{ls}$ ($\Delta E_{R.E}=+123.9$ kJ mol^{-1}).

Conclusion

A new family of nickel(II) complexes of pentadentate N5 ligands has been isolated, characterized, and their ability to carry out alkane hydroxylation by using *m*-CPBA as oxidant has been studied. The X-ray crystal structure of one of these complexes possesses a distorted octahedral nickel(II) coordination geometry constituted by the N5 ligand and one solvent molecule. The UV/Vis spectra reveal an octahedral coordination geometry for all of the complexes in solution. All the complexes catalyze the oxidation of cyclohexane, adamantane, and cumene with high TONs and selectivity. Interestingly, the nickel(II) complex with a strongly π-backbonding pyridine nitrogen atom acts as an efficient catalyst towards oxidation of alkanes by stabilizing the high-valent reactive nickel-oxo intermediate species, whereas that with a good σ-donating imidazole nitrogen atom acts as a less efficient catalyst by destabilizing the reactive intermediate. The computed results show that the high-spin ($S=3/2$) $[(5N)Ni^{II}–O^{\bullet}]^{+}$ species is found to be the ground state with the low-spin ($S=1/2$) excited state located close to it. The cyclohexane hydroxylation occurs through a major pathway involving the high-spin $[(5N)Ni^{II}–O^{\bullet}]^{+}$ species and two transition states, $ts1_{hs}$ and $ts2_{doublet}$. However, a minor pathway for the same species but with a low-spin state and two transition states, $ts1_{ls}$ and $ts2_{doublet}$ may also operate because both the high-spin and low-spin $[(5N)Ni^{II}–O^{\bullet}]^{+}$ species coexist with a small energy gap for the spin cross over. Overall, a two spin-state reactivity is predicted for the $[(5N)Ni^{II}–O^{\bullet}]^{+}$-catalyzed cyclohexane hydroxylation reactions wherein the rate-determining step is the hydrogen abstraction. Also, the DFT studies illustrate that if the homolytic O–O bond cleavage of the peroxo species $[Ni^{II}(L)(OOCOC_6H_4Cl)]^{+}$ to form the reactive $[(L)Ni^{II}–O^{\bullet}]^{+}$ intermediate is thermodynamically less favored then the catalytic activity would be decreased. The catalytic ability of the present Ni(N5) complexes are lower than those of Ni(N4) complexes suggesting that at least two coordination sites are needed for conferring a better catalytic efficiency on the complexes. The present study also suggests that a robust Ni^{II} catalyst for alkane oxidation may be designed by incorporating strongly π-backbonding heterocyclic nitrogen donor atoms on a tetradentate ligand.

Experimental Section

Materials

Pyridine-2-carboxaldehyde, *N*-methylethylenediamine, *N*-benzylethylenediamine, nickel(II) perchlorate hexahydrate, adamantane, cumene, *m*-chloroperbenzoic acid, sodium tetraphenylborate, sodium borohydride, 1-methylimidazole-2-carboxldehyde, tetra-*N*-butylammonium bromide (Aldrich), 6-methylpyridine-2-carboxldehyde, quinoline-2-carboxaldehyde, sodium triacetoxyborohydride (Alfa Aesar), acetic acid glacial, ethyl acetate, triethylamine, sodium sulphate (Merck, India), and cyclohexane (Ranbaxy) were used as received. Dichloromethane, diethyl ether, tetrahydrofuran, acetonitrile (Merck, India), and methanol (Sisco Research Laboratory, Mumbai) were distilled before use. The supporting electrolyte tetra-*N*-butylammonium perchlorate (TBAP) was prepared in water and re-crystallized twice from aqueous ethanol.

Synthesis of the ligands

***N*-Methyl-*N*,*N*′,*N*′-tris(pyrid-2-ylmethyl)ethylenediamine (L1)**: The ligand was prepared as reported[42] elsewhere. Yield: 1.39 g (80%); ^{1}H NMR (400 MHz, $CDCl_3$): $\delta=2.28$ (s, 3H; NCH_3), 2.54–2.77 (m, 4H; NCH_2CH_2N), 3.70 (s, 2H; NCH_2 of pyridyl), 3.90 (s, 4H; NCH_2 of pyridyl), 7.00–8.56 ppm (m, 12H; pyridyl); ^{13}C NMR (400 MHz, $CDCl_3$): $\delta=159.21$, 148.63, 148.58, 135.81, 122.52, 122.37, 121.43, 121.36, 63.33, 60.26, 55.03, 51.55, 42.19 ppm; MS (EI): *m/z* calcd for $C_{21}H_{25}N_5^+$: 347.21; found: 347.3.

***N*-Benzyl-*N*,*N*′,*N*′-tris(pyrid-2-ylmethyl)ethylenediamine (L2)**: The ligand was prepared as reported[43] elsewhere. Yield: 1.25 g (59%); ^{1}H NMR (400 MHz, $CDCl_3$): $\delta=2.60$–2.70 (m, 4H; $2\times CH_2$), 3.53 (s,

© 2014 Wiley-VCH Verlag GmbH & Co. KGaA, Weinheim

2H; CH_2), 3.68 (s, 2H; CH_2), 3.73 (s, 4H; 2×CH_2), 7.05–7.10 (m, 3H), 7.19–7.22 (m, 5H), 7.39–7.41 (m, 3H), 7.56–7.66 (m, 3H), 8.42–8.51 ppm (m, 3H; Py, Ar); ^{13}C NMR (400 MHz, $CDCl_3$): δ = 160.09, 159.65, 148.85, 148.70, 139.11, 136.22, 128.64, 128.09, 126.79, 122.64, 122.59, 121.75, 121.69, 60.71, 60.65, 60.51, 58.91, 52.15, 51.83 ppm; MS (EI): *m/z* calcd for $C_{27}H_{29}N_5^+$: 423.24; found: 423.3.

***N*-Methyl-*N*,*N*′-bis(pyrid-2-ylmethyl)-*N*′-(6-methylpyrid-2-ylmethyl)ethylenediamine (L3)**: Step I: *N*-Methyl-*N*′-(6-methylpyrid-2-ylmethyl)ethylenediamine was synthesized by adding 6-methylpyridine-2-carboxaldehyde (0.619 g, 5 mmol) in methanol (20 mL) to *N*-methyl-ethylenediamine (0.780 g, 10 mmol) in methanol (20 mL) and then stirring the solution for twelve hours. Then the solution was cooled to 0 °C and sodium borohydride (7.5 mmol) was added and the stirring continued for twelve hours. The solvent was removed under vacuum, the residue was extracted by using ethyl acetate and the water was removed by using sodium sulphate. The solvent was removed under vacuum to give a pale yellow oil, which was used for the preparation of L2 without further purification.

Step II: To a mixture of *N*-methyl-*N*′-(6-methylpyrid-2-ylmethyl)ethylenediamine (0.895 g, 5 mmol), pyridine-2-carboxaldehyde (1.08 g, 10 mmol), and acetic acid glacial (570 μL, 10 mmol) in tetrahydrofuran (50 mL) was added sodium triacetoxyborohydride (3.75 g, 17.7 mmol) and the solution was stirred for 48 h. The reaction was quenched with saturated sodium hydrogencarbonate solution and extracted with ethyl acetate. The organic fractions were combined, dried (Na_2SO_4), and the solvent was removed under reduced pressure to obtain the product. The yellow oil obtained was purified by using flash chromatography and then used for complex preparation. Yield: 1.60 g (88%); ^{1}H NMR (400 MHz, $CDCl_3$): δ = 2.29 (s, 3H; NCH_3), 2.76–2.80 (m, 4H; NCH_2CH_2N), 2.59 (s, 3H; CH_3), 3.71 (s, 2H; NCH_2 of pyridyl), 3.92 (s, 4H; NCH_2 of pyridyl), 7.00–8.60 ppm (m, 11H; pyridyl); ^{13}C NMR (400 MHz, $CDCl_3$): δ = 159.26, 148.69, 148.68, 135.61, 122.32, 122.27, 121.33, 121.32, 63.23, 60.22, 55.13, 51.45, 42.12, 28.51 ppm; MS (EI): *m/z* calcd for $C_{22}H_{27}N_5^+$: 361.23: found: 361.3.

***N*-Methyl-*N*,*N*′-bis(pyrid-2-ylmethyl)-*N*′-(quinolin-2-ylmethyl)ethylenediamine (L4)**: The procedure employed for the preparation of L3 was used for obtaining L4 and quinoline-2-carboxaldehyde was used instead of pyridine-2-carboxaldehyde. The brown oil was purified by using flash chromatography and the obtained product was used for complex preparation. Yield: 1.41 g (71%); ^{1}H NMR (400 MHz, $CDCl_3$): δ = 2.29 (s, 3H; NCH_3), 2.76–2.82 (m, 4H; NCH_2CH_2N,), 3.73 (s, 2H; NCH_2 of quinolyl), 3.94 (s, 4H;NCH_2 of pyridyl), 7.00–8.56 ppm (m, 14H; aromatic); ^{13}C NMR (400 MHz, $CDCl_3$): δ = 159.23, 148.62, 148.38, 135.51, 129.86, 128.61, 127. 32, 125. 80, 122.31, 122.29, 121.34, 121.39, 63.13, 60.22, 60.56, 55.15, 51.45, 42.11 ppm; MS (EI): *m/z* calcd for $C_{25}H_{27}N_5^+$: 397.23; found: 397.3.

***N*-Methyl-*N*,*N*′-bis(pyrid-2-ylmethyl)-*N*′-(imidazole-2-ylmethyl)ethylenediamine (L5)**: The procedure employed for the preparation of L1 was used for L5 and imidazole-2-carboxaldehyde was used instead of pyridine-2-carboxaldehyde. The colorless oil was purified by using flash chromatography and the obtained product was used for complex preparation. Yield: 1.36 g (78%);^{1}H NMR (400 MHz, $CDCl_3$): δ = 2.29 (s, 3H; NCH_3), 2.76–2.81 (m, 4H; NCH_2CH_2N), 3.59 (s, 3H; NCH_3), 3.71 (s, 2H; NCH_2 of imidazolyl), 3.91 (s, 4H; NCH_2 of pyridyl), 6.70–8.56 ppm (m, 10H; pyridyl); ^{13}C NMR (400 MHz, $CDCl_3$): δ = 156.21, 152.14, 148.67, 135.63, 127.35, 124.23, 120.34, 120.37, 62.21, 60.27, 53.11, 51.44, 48.92, 42.14, 28.56 ppm; MS (EI): *m/z* calcd for $C_{20}H_{26}N_6^+$: 350.22; found: 350.3.

Synthesis of the Ni^{II} complexes

[Ni(L1)(CH_3CN)](BPh_4)$_2$ (1): A solution of [Ni(ClO_4)$_2$]·6H_2O (0.365 g, 1 mmol) in methanol (5 mL) was added to a solution of L1 (0.347 g, 1 mmol) in methanol (5 mL) with stirring at room temperature when the color of the solution turned to indigo. After stirring the solution for 30 min, acetonitrile (5 mL) was added. The solution was stirred for additional 30 min when the color of the solution turned blue. Upon metathesis of the complex by adding $NaBPh_4$ (0.684 g, 2 mmol) in methanol (3 mL), a pink-colored precipitate was obtained, which was filtered off, washed with small quantities of ice-cold methanol and then dried. Yield, 0.91 g (84%); MS (ESI): *m/z*: 202.67 $[M-CH_3CN-2BPh_4]^{2+}$; elemental analysis calcd (%) for $C_{71}H_{68}N_6B_2Ni$: C 78.55, H 6.31, N 7.74; found: C 78.63, H 6.42, N 7.79.

[Ni(L2)(CH_3CN)](BPh_4)$_2$ (2): A procedure analogous to that used to prepare complex **1** was followed by using L2 (0.423 g, 1 mmol) instead of L1. The pure product was isolated as a purple precipitate. Yield: 0.94 g (81%); MS (ESI): *m/z*: 240.67 $[M-CH_3CN-2BPh_4)^{2+}$; elemental analysis calcd (%) for $C_{77}H_{72}N_6B_2Ni$: C 79.61, H 6.25, N 7.23; found: C 79.56, H 6.33, N 7.31.

[Ni(L3)(CH_3CN)](BPh_4)$_2$ (3): This complex was prepared by using a procedure analogous to that used to prepare complex **1** and L3 (0.361 g, 1 mmol) was used instead of L1. The pure product was isolated as a purple precipitate. Yield 0.86 g (78%); MS (ESI): *m/z*: 209.67 $[M-CH_3CN-2BPh_4]^{2+}$; elemental analysis calcd for $C_{72}H_{70}N_6B_2Ni$: C 78.64, H 6.42, N 7.64; found: C 78.56, H 6.57, N 7.72. Single crystals suitable for X-ray crystallographic analysis were obtained by slow evaporation of a solution of the complex in a dichloromethane/acetonitrile solvent mixture.

[Ni(L4)(CH_3CN)](BPh_4)$_2$ (4): A procedure analogous to that used to prepare complex **1** was used and L4 (0.397 g, 1 mmol) was used instead of L1. The pure product was isolated as a purple precipitate. Yield 0.81 g (71%); MS (ESI): *m/z*: 234.48 $[M-CH_3CN-2BPh_4]^{2+}$; elemental analysis calcd for $C_{75}H_{70}N_6B_2Ni$: C 79.32, H 6.21, N 7.40; found: C 79.28, H 6.28, N 7.20.

[Ni(L5)(CH_3CN)](BPh_4)$_2$ (5): This complex was isolated by employing the procedure analogous to that used to prepare complex **1** and by using L5 (0.350 g, 1 mmol) instead of L1. The pure product was isolated as a purple precipitate. Yield 0.87 g (80%); MS (ESI): *m/z*: 224.07 $[M-CH_3CN-2BPh_4]^{2+}$; elemental analysis calcd for $C_{70}H_{69}N_7B_2Ni$: C 77.23, H 6.39 N 9.01; found: C 77.35, H 6.31, N 9.11.

Caution!

Perchlorate salts of the compounds are potentially explosive. Only small quantities of these compounds should be prepared and suitable precautions should be taken when they are handled.

Catalytic oxidations

The oxidation of alkanes was carried out under a nitrogen atmosphere at room temperature within two hours. In a typical reaction, the nickel(II) complex (0.35×10^{-3} mmol dm^{-3}) was added to a mixture of alkanes (2.45 mol dm^{-3}) and oxidant *m*-CPBA (0.35 mol dm^{-3}) in a CH_2Cl_2:CH_3CN mixture (3:1 v/v). After 2 h the reaction mixture was quenched with triphenylphosphine and filtered over a silica column and then eluted with diethyl ether. An internal standard (bromobenzene) was added at this point and the solution was subjected to GC analysis. The mixture of organic products were identified by Agilent GC-MS and quantitatively analyzed by HP 6890 series GC equipped with a HP-5 capillary column

© 2014 Wiley-VCH Verlag GmbH & Co. KGaA, Weinheim

(30 m×0.32 mm×2.5 μm) by using a calibration curve obtained with authentic compounds. All of the products were quantified by using GC (FID) with the following temperature program: injector temperature = 130 °C, initial temperature = 60 °C, heating rate = 10 °C min^{-1} to 130 °C, increasing the temperature to 160 °C at a rate of 2 °C min^{-1}, and then increasing the temperature to 260 °C at a rate of 5 °C min^{-1}, FID temperature = 280 °C. GC-MS analysis was performed under conditions identical to those used for GC analysis. The averages of three measurements are reported.

Physical measurements

Elemental analyses were performed on a Perkin–Elmer Series II CHNS/O Analyzer 2400. ^{1}H NMR spectra were recorded on a Bruker 400 MHz NMR spectrometer. All the ligands were purified on TELEDYNE CombiFlash R_f Flash chromatography. Electronic spectra were recorded on a Agilent 8453 Diode Array Spectrophotometer. Low-temperature spectra were obtained on a Agilent 8453 Diode Array Spectrophotometer equipped with an UNISOKU USP-203 cryostat. ESI-MS analyses were recorded on a Micromass Quattro II triple quadrupole mass spectrometer. Cyclic voltammetry (CV) and differential pulse voltammetry (DPV) were performed at (25 ± 0.2) °C by using a three-electrode cell configuration. A platinum sphere, a platinum plate, and Ag(s)/$AgNO_3$ were used as working, auxiliary, and reference electrodes, respectively. The platinum sphere electrode was sonicated for two minutes in dilute nitric acid, dilute hydrazine hydrate, and in double distilled water to remove the impurities. The reference electrode for non-aqueous solution was Ag(s)/Ag^+, which consists of a Ag wire immersed in a solution of $AgNO_3$ (0.01 M) and tetra-*N*-butylammonium perchlorate (0.1 M) in acetonitrile placed in a tube fitted with a vycor plug. The instruments utilized included an EG & G PAR 273 Potentiostat/Galvanostat and P-IV computer along with EG & G M270 software to carry out the experiments and to acquire the data. The temperature of the electrochemical cell was maintained by a cryo-circulator (HAAKE D8-G). The $E_{1/2}$ value observed under identical conditions for the ferrocene/ferrocenium (Fc/Fc^+) couple in acetonitrile was 0.102 V with respect to the Ag/Ag^+ reference electrode. The experimental solutions were deoxygenated by bubbling research-grade nitrogen and an atmosphere of nitrogen was maintained over the solution during measurements. The products were analyzed by using a Hewlett Packard (HP) 6890 GC series Gas Chromatograph equipped with a FID detector and a HP-5 capillary column (30 m× 0.32 mm×2.5 μm). GC-MS analysis was performed on an Agilent GC-MS equipped with 7890A GC series (HP-5 capillary column) and 5975C inert MSD under conditions that are identical to that used for GC analysis.

Crystallographic data collection, refinement, and structure solution

The diffraction experiments were carried out on a Bruker SMART APEX diffractometer equipped with a CCD area detector. High-quality crystals, suitable for X-ray diffraction were chosen after careful examination under an optical microscope. Intensity data for the crystals were collected by using $Mo_{K\alpha}$ ($\lambda = 0.71073$ Å) radiation on a Bruker SMART APEX diffractometer equipped with a CCD area detector at 296 K. The structure was solved by direct methods by using the SHELXS-97.[50] The refinement and all further calculations were carried out by using SHELXL-97.[51] The SMART[52] program was used for collecting frames of data, indexing reflection, and determination of lattice parameters; the SAINT[52] program was used for integration of the intensity of reflections and scaling; the SADABS[53] program was used for absorption correction, and the SHELXTL[54] program was used for space group and structure determination, and least-squares refinements on F^2. The structure was solved by the heavy-atom method and other non-hydrogen atoms were located in successive difference Fourier syntheses. After locating the Ni^{II} complex with the bulky anions, interlinked diffused peaks with residual electron density ranging from 2.3–1.5 e Å^{-3} were observed in the difference Fourier map, which can be attributed to disordered solvent molecule (acetonitrile used for crystallization) present in the crystal lattice. Attempts were made to model these residual electron density peaks, but were unsuccessful because the peaks obtained were diffused and there was no obvious major site occupations for the solvent molecules. The PLATON/SQUEEZE[55] option has been used to correct the data for the contribution from of the disordered solvent. Final cycles of least-squares refinements with the modified data set improved both the *R* values and the goodness of fit significantly. Crystal data and additional details of the data collection and refinement of the structure are presented in Table 8. The selected bond lengths and bond angles are listed in Table 1. CCDC 898033 contains the supplementary crystallographic data for complex **3**. These data can be obtained free of charge from The Cambridge Crystallographic Data Centre via www.ccdc.cam.ac.uk/data_request/cif.

Table 8. Crystallographic data for complex **3**.

empirical formula	$C_{72}H_{70}B_2N_6Ni$
formula weight [g mol^{-1}]	1099.67
crystal habit, color	pink
crystal system	monoclinic
crystal size [mm^3]	0.08×0.08×0.07
space group	*P*21/*c*
a [Å]	22.0950(5)
b [Å]	17.3654(4)
c [Å]	18.4523(5)
α [°]	90
β [°]	102.842(10)
g [°]	90
V [Å^{-3}]	6902.8(3)
Z	4
ρ_{calcd} [g cm^{-3}]	1.058
F(000)	2328
temperature [K]	293(2)
no. of reflns collected	128631
no. of unique reflns	14792 (R(int) = 0.0433)
radiation ($Mo_{K\alpha}$) [Å]	0.71073
goodness-of-fit on F^2	1.084
no. of refined parameters	726
$R1$/w$R2$[$I > 2\sigma(I)$][a]	$R_1 = 0.0437$, $wR_2 = 0.1295$
$R1$/w$R2$ (all data)	$R_1 = 0.0608$, $wR_2 = 0.1368$

[a] $R1 = [\Sigma(||F_o|-|F_c||)/\Sigma|F_o|]$; $wR2 = \{[\Sigma(w(F_o^2-F_c^2)^2)/\Sigma(wF_o^4)]^{1/2}\}$.

Computational details

In the current study, all geometries are fully optimized by the B3LYP-DFT method by using the Gaussian 09 program.[56] The calculations were carried out with a mixed basis set (B1) of LanL2DZ for the Ni center, which has a relativistic effective core potential with a valence basis set and 6-31G** for the remaining atoms.[57] All the intermediates were confirmed by the frequency calculations as minima on the potential energy surface. The transition states were characterized by a single negative frequency and verified further by animating the frequency that correspond to the C–H bond elongation/C–O bond formation, as concern to this study. For se-

© 2014 Wiley-VCH Verlag GmbH & Co. KGaA, Weinheim

lected transition states, intrinsic reaction coordinate (IRC) calculations were preformed to confirm that the transition state is indeed connected to the corresponding reactant and the product in the potential energy surface. Further, to get the reliable energetics, single-point calculations were performed on the B3LYP/B1-optimized geometries by using LanL2DZ for the Ni center and 6-311++G** for the remaining atoms (basis set B2). The quoted energies are those calculated at the B3LYP/B2//B3LYP/B1 level, including the free energy corrections obtained from the B3LYP/B1-optimized geometries. In addition, the single-point calculations at B3LYP/B1 have also been performed with all electron TZVP basis sets for all atoms (free energy corrections obtained from the B3LYP/B1-optimized geometries) for representative systems. This has been compared with the B3LYP/B2//B3LYP/B1 energies (see Table S2 in the Supporting Information). The B3LYP/TZVP//B3LYP/B1 level energetics are found to be very close to the B3LYP/B2//B3LYP/B1 energetics (up to the variation of 3–6 kJ mol^{-1}). Hence, the B3LYP/B2//B3LYP/B1 free energies are discussed throughout in the text unless otherwise mentioned. It is known that there are instances that B3LYP predicts incorrect ground states, especially for systems having small low-spin and high-spin gaps.[58] In the case of [(L1)Ni^{II}–O$^{\bullet}$] and [(L5)Ni^{II}–O$^{\bullet}$], the high-spin ($S=3/2$) and low-spin ($S=1/2$) energy gap is found to be +25.1 and +16.2 kJ mol^{-1}, respectively, at the B3LYP/B2//B3LYP/B1 level. Hence, the structure optimization of [(L1/L5)Ni^{II}–O$^{\bullet}$] species was carried out with six other DFT methods, namely, B3LYP-D, wB97XD, B97D, M06-2X, B3LYP*, and B3LYP** along with single-point calculations by using TPSSh and OLYP methods[48] to confirm the ground-state spin configuration. Previously, Shaik et al. have performed a method assessment for the hydrogen-abstraction reaction of non-heme model complex by using the RCCSD(T) and B3LYP and B3LYP-D along with TPSSh functionals and were able to predict the spin-state energetics close to those found with the RCCSD(T) method.[59] For spin-coupled states Noodlemann's broken-symmetry method was employed to obtain the correct polarized spin states. To aid smooth convergence of radical intermediates, fragment approach in Gaussian 09 were used. To study the effect of the solvent (CH_3CN), single-point B3LYP/B2 level calculation on the B3LYP/B1-optimized geometries have also been performed with the polarized continuum model (PCM).[60] With solvation correction, the maximum change in the relative energy of the optimized structures is not more than 12 kJ mol^{-1}[61] and also the trend in the energetics with and without solvation effects is similar to the B3LYP/B2//B3LYP/B1 level. Hence, the effect of CH_3CN as solvent is neglected in the data discussed here.

Acknowledgements

We sincerely thank the Council of Scientific and Industrial Research, New Delhi, for a Senior Research Fellowship to M.S. and the Department of Science & Technology, SERB, for the award of Fast track Young Scientist Fellowship to P.V. (Ref. No: CS-232/2012). This work was supported by the DST Nano Mission. Project (SR/NM/NS-110/2010 (G)) and a CSIR project (CSIR/01(2462)/11/EMR-II). Professor M. Palaniandavar is a recipient of the DST Ramanna Fellowship [Scheme No. SR/S1/RFIC-01/2007 and SR/S1/RFIC-01/2010]. We also thank the Director of the National Institute for Interdisciplinary Science and Technology (NIIST)-CSIR, Trivandrum, for providing the computational facility. We thank the Department of Science and Technology (FIST program), New Delhi for the use of the X-ray diffractometer at the School of Chemistry. We thank Dr. Balachandran Unni Nair, Central Leather Research Institute, Chennai for providing the ESI-MS facility.

Keywords: density functional calculations · hydroxylation · N ligands · nickel · Ni–O$^{\bullet}$ species

[1] D. Riley, M. Stern, J. Ebner in *The Activation of Dioxygen and Homogeneous Catalytic Oxidation* (Eds.: D. H. R. Barton, A. E. Martell, D. T. Sawyer), Plenum Press, New York, **1993**, p. 31.
[2] M. Costas, K. K. Chen, L. Que, Jr., *Coord. Chem. Rev.* **2000**, *200*, 517.
[3] D. H. R. Barton, D. Doller, *Acc. Chem. Res.* **1992**, *25*, 504.
[4] A. E. Shilov, A. A. Shteinman, *Acc. Chem. Res.* **1999**, *32*, 763.
[5] P. Stavropoulos, R. Çelenligil-Çetin, A. E. Tapper, *Acc. Chem. Res.* **2001**, *34*, 745.
[6] T. Punniyamurthy, S. Velusamy, J. Iqbal, *Chem. Rev.* **2005**, *105*, 2329.
[7] K. Nehru, S. J. Kim, I. Y. Kim, M. S. Seo, Y. Kim, S. Kim, J. Kim, W. Nam, *Chem. Commun.* **2007**, 4623.
[8] F. A. Chavez, P. K. Mascharak, *Acc. Chem. Res.* **2000**, *33*, 539.
[9] L. M. Mirica, X. Ottenwaelder, T. D. P. Stack, *Chem. Rev.* **2004**, *104*, 1013.
[10] L. Que, Jr., W. B. Tolman, *Angew. Chem. Int. Ed.* **2002**, *41*, 1114.
[11] C. J. Cramer, W. B. Tolman, *Acc. Chem. Res.* **2007**, *40*, 601.
[12] T. Kojima, *Chem. Lett.* **1996**, 121.
[13] T. Kojima, H. Matsuo, Y. Matsuda, *Inorg. Chim. Acta* **2000**, *300–302*, 661.
[14] J. R. Bryant, T. Matsuo, J. M. Mayer, *Inorg. Chem.* **2004**, *43*, 1587.
[15] M. Yamaguchi, H. Kousaka, S. Izawa, Y. Ichii, T. Kumano, D. Masui, T. Yamagishi, *Inorg. Chem.* **2006**, *45*, 8342.
[16] T. Kojima, K. Hayashi, S. Iizuka, F. Tani, Y. Naruta, M. Kawano, Y. Ohashi, Y. Hirai, K. Ohkubo, Y. Matsuda, S. Fukuzumi, *Chem. Eur. J.* **2007**, *13*, 8212.
[17] S. Yiu, W. Man, T. Lau, *J. Am. Chem. Soc.* **2008**, *130*, 10821.
[18] a) D. Schröder, H. Schwarz, *Angew. Chem.* **1995**, *107*, 2126; *Angew. Chem. Int. Ed. Engl.* **1995**, *34*, 1973; b) K. Jitsukawa, Y. Oka, S. Yamaguchi, H. Masuda, *Inorg. Chem.* **2004**, *43*, 8119; c) M. Murali, R. Mayilmurugan, M. Palaniandavar, *Eur. J. Inorg. Chem.* **2009**, 3238.
[19] S. Itoh, H. Bandoh, S. Nagatomo, T. Kitagawa, S. Fukuzumi, *J. Am. Chem. Soc.* **1999**, *121*, 8945.
[20] S. Itoh, H. Bandoh, M. Nakagawa, S. Nagatomo, T. Kitagawa, K. D. Karlin, S. Fukuzumi, *J. Am. Chem. Soc.* **2001**, *123*, 11168.
[21] M. Suzuki, *Acc. Chem. Res.* **2007**, *40*, 609.
[22] S. Hikichi, M. Yoshizawa, Y. Sasakura, H. Komatsuzaki, Y. Moro-oka, M. Akita, *Chem. Eur. J.* **2001**, *7*, 5011.
[23] M. T. Kieber-Emmons, C. G. Riordan, *Acc. Chem. Res.* **2007**, *40*, 618.
[24] J. F. Kinneary, J. S. Albert, C. J. Burrows, *J. Am. Chem. Soc.* **1988**, *110*, 6124.
[25] S. Hikichi, M. Yoshizawa, Y. Sasakura, M. Akita, Y. Moro-oka, *J. Am. Chem. Soc.* **1998**, *120*, 10567.
[26] K. Shiren, S. Ogo, S. Fujinami, H. Hayashi, M. Suzuki, A. Uehara, Y. Watanabe, Y. Moro-oka, *J. Am. Chem. Soc.* **2000**, *122*, 254.
[27] B. S. Mandimutsira, J. L. Yamarik, T. C. Brunold, W. Gu, S. P. Cramer, C. G. Riordan, *J. Am. Chem. Soc.* **2001**, *123*, 9194.
[28] K. Fujita, R. Schenker, W. Gu, T. C. Brunold, S. P. Cramer, C. G. Riordan, *Inorg. Chem.* **2004**, *43*, 3324.
[29] J. Cho, H. Furutachi, S. Fujinami, M. Suzuki, *Angew. Chem.* **2004**, *116*, 3362; *Angew. Chem. Int. Ed.* **2004**, *43*, 3300.
[30] M. T. Kieber-Emmons, J. Annaraj, M. S. Seo, K. M. Van Heuvelen, T. Tosha, T. Kitagawa, T. C. Brunold, W. Nam, C. G. Riordan, *J. Am. Chem. Soc.* **2006**, *128*, 14230.
[31] S. Yao, E. Bill, C. Milsmann, K. Wieghardt, M. Driess, *Angew. Chem.* **2008**, *120*, 7218; *Angew. Chem. Int. Ed.* **2008**, *47*, 7110.
[32] A. Company, S. Yao, K. Ray, M. Driess, *Chem. Eur. J.* **2010**, *16*, 9669.
[33] S. Hikichi, C. Kobayashi, M. Yoshizawa, M. Akita, *Chem. Asian J.* **2010**, *5*, 2086.
[34] T. Tano, Y. Doi, M. Inosako, A. Kunishita, M. Kubo, H. Ishimaru, T. Ogur, H. Sugimoto, S. Itoh, *Bull. Chem. Soc. Jpn.* **2010**, *83*, 530.
[35] a) Y. Shiota, K. Yoshizawa, *J. Am. Chem. Soc.* **2000**, *122*, 12317; b) A. W. Pierpont, T. R. Cundari, *Inorg. Chem.* **2010**, *49*, 2038.
[36] T. Nagataki, Y. Tachi, S. Itoh, *Chem. Commun.* **2006**, 4016.
[37] T. Nagataki, K. Ishii, Y. Tachi, S. Itoh, *Dalton Trans.* **2007**, 1120.
[38] T. Nagataki, S. Itoh, *Chem. Lett.* **2007**, *36*, 748.

 © 2014 Wiley-VCH Verlag GmbH & Co. KGaA, Weinheim

[39] a) S. Hikichi, H. Okuda, Y. Ohzu, M. Akita, *Angew. Chem.* **2009**, *121*, 194; *Angew. Chem. Int. Ed.* **2009**, *48*, 188; b) S. Hikichi, K. Hanaue, T. Fujimura, H. Okuda, J. Nakazawa, Y. Ohzu, C. Kobayashi, M. Akita, *Dalton Trans.* **2013**, *42*, 3346; c) J. Nakazawa, S. Terada, M. Yamada, S. Hikichi, *J. Am. Chem. Soc.* **2013**, *135*, 6010.

[40] a) M. Balamurugan, R. Mayilmurugan, E. Suresh, M. Palaniandavar, *Dalton Trans.* **2011**, *40*, 9413; b) M. Sankaralingam, P. Vadivelu, E. Suresh, M. Palaniandavar, *Inorg. Chim. Acta* **2013**, *407*, 98.

[41] F. F. Pfaff, F. Heims, S. Kundu, S. Mebs, K. Ray, *Chem. Commun.* **2012**, *48*, 3730.

[42] a) P. A. MacFaul, I. W. C. E. Arends, K. U. Ingold, D. D. M. Wayner, *J. Chem. Soc. Perkin Trans. 1* **1997**, *2*, 135; b) I. Bernal, I. M. Jensen, K. B. Jensen, C. J. McKenzie, H. Toftlund, J. P. Tuchagues, *J. Chem. Soc. Dalton Trans.* **1995**, 3667.

[43] a) M. Lubben, A. Meetsma, E. C. Wilkinson, B. L. Feringa, L. Que, Jr., *Angew. Chem.* **1995**, *107*, 1610; *Angew. Chem. Int. Ed. Engl.* **1995**, *34*, 1512; b) L. Duelund, R. Hazell, C. J. McKenzie, L. P. Nielsen, H. Toftlund, *J. Chem. Soc. Dalton Trans.* **2001**, 152.

[44] a) M. Velusamy, M. Palaniandavar, K. R. Justin Thomas, *Polyhedron* **1998**, *17*, 2179; b) A. B. P. Lever, *Inorganic Electronic Spectroscopy*, 2ednd edElsevier, Amsterdam, **1986**.

[45] J. C. Brodovitch, R. I. Haines, A. Mcauley, *Can. J. Chem.* **1981**, *59*, 1610.

[46] A. Bravo, H.-R. Bjorsvik, F. Fontana, F. Minisci, A. Serri, *J. Org. Chem.* **1996**, *61*, 9409.

[47] a) P. Comba, M. Maurer, P. Vadivelu, *J. Phys. Chem. A* **2008**, *112*, 13028; b) P. Comba, M. Maurer, P. Vadivelu, *Inorg. Chem.* **2009**, *48*, 10389.

[48] A. Ansari, A. Kaushik, G. Rajaramam, *J. Am. Chem. Soc.* **2013**, *135*, 4235.

[49] P. E. M. Siegbahn, *J. Comput. Chem.* **2001**, *22*, 1634.

[50] SHELXS-97 Program for Crystal Structure Determination: G. M. Sheldrick, *Acta Crystallogr.* **1990**, *A46*, 467 – 473.

[51] SHELXL-97, G. M. Sheldrick, Universität Göttingen, Göttingen (Germany), **1999**.

[52] SAINT 5.1 ed., G. M. Sheldrick, Siemens Industrial Automation Inc., Madison, WI, **1995**.

[53] SADABS. Program for Empirical Absorption Correction of Area Detector, G. M. Sheldrick, University of Göttingen, Göttingen (Germany), **1996**.

[54] SHELXTL V5.1 Software Reference Manual, G. M. Sheldrick, Bruker AXS, Inc., Madison, Wisconsin, USA.

[55] A. L. Spek, *Acta Crystallogr. Sect. C* **1990**, *34*, 46.

[56] Gaussian 09, Revision A.1, M. J. Frisch, G. W. Trucks, H. B. Schlegel, G. E. Scuseria, M. A. Robb, J. R. Cheeseman, G. Scalmani, V. Barone, B. Mennucci, G. A. Petersson, H. Nakatsuji, M. Caricato, X. Li, H. P. Hratchian, A. F. Izmaylov, J. Bloino, G. Zheng, J. L. Sonnenberg, M. Hada, M. Ehara, K. Toyota, R. Fukuda, J. Hasegawa, M. Ishida, T. Nakajima, Y. Honda, O. Kitao, H. Nakai, T. Vreven, J. A. Montgomery, Jr., J. E. Peralta, F.Ogliaro, M. Bearpark, J. J. Heyd, E. Brothers, K. N. Kudin, V. N. Staroverov, R. Kobayashi, J. Normand, K. Raghavachari, A. Rendell, J. C. Burant, S. S. Iyengar, J. Tomasi, M. Cossi, N. Rega, J. M. Millam, M. Klene, J. E. Knox, J. B. Cross, V. Bakken, C. Adamo, J. Jaramillo, R. Gomperts, R. E. Stratmann, O. Yazyev, A. J. Austin, R. Cammi, C. Pomelli, J. W. Ochterski, R. L. Martin, K. Morokuma, V. G. Zakrzewski, G. A. Voth, P. Salvador, J. J. Dannenberg, S. Dapprich, A. D. Daniels, Ö. Farkas, J. B. Foresman, J. V. Ortiz, J. Cioslowski, D. J. Fox, Gaussian, Inc., Wallingford CT, **2009**.

[57] a) A. D. Becke, *J. Chem. Phys.* **1993**, *98*, 1372; b) P. J. Hay, W. R. Wadt, *J. Chem. Phys.* **1985**, *82*, 270; c) P. J. Hay, W. R. Wadt, *J. Chem. Phys.* **1985**, *82*, 299.

[58] a) K. Boguslawski, C. R. Jacob, M. Reiher, *J. Chem. Theory Comput.* **2011**, *7*, 2740; b) K. P. Kepp, *Coord. Chem. Rev.* **2013**, *257*, 196; c) S. Ye, F. Neese, *Inorg. Chem.* **2010**, *49*, 772.

[59] H. Chen, W. Lai, S. Shaik, *J. Phys. Chem. Lett.* **2010**, *1*, 1533.

[60] a) M. T. Cancès, B. Mennucci, J. Tomasi, *J. Chem. Phys.* **1997**, *107*, 3032; b) M. Cossi, B. Barone, B. Mennucci, J. Tomasi, *J. Chem. Phys. Lett.* **1998**, *286*, 253; c) B. Mennucci, J. Tomasi, *J. Chem. Phys.* **1997**, *106*, 5151; d) M. Cossi, G. Scalmani, N. Raga, V. Barone, *J. Chem. Phys.* **2002**, *117*, 43.

[61] P. Comba, M. Maurer, P. Vadivelu, *J. Phys. Chem. A* **2008**, *112*, 13028.

Received: February 27, 2014
Published online on August 5, 2014

© 2014 Wiley-VCH Verlag GmbH & Co. KGaA, Weinheim